Master's Thesis of Natural Science

Sensitivity analysis of ice dynamics to climate forcing scenarios in David Glacier, East Antarctica

기후 변화 시나리오에 따른 데이비드 빙하 빙상 거동 민감도 분석

February 2018

Graduate School of School of Earth and Environmental Sciences

Seoul National University

Park, In Woo

Abstract

As global mean temperature rises, there has been a growing interest in how much sea level would rise occurred due to polar glacial discharge to ocean. Currently, West Antarctica has been spotlighted due to ice discharge from the glaciers, compared to sea level contribution in East Antarctic glaciers. Bed elevation at East Antarctica is largely lying above sea level, which is likely to stable compared to West Antarctica. However, East Antarctic regions contain 10 times large sea level rise potential than West Antarctica. David Glacier, located in East Antarctica, is a region of fjord-like valley glacier, and ice drains into ocean through Drygalski Ice Tongue, which of length is about 80 km. To understand what mechanism modulates sea level rise, it is necessary to identify key factors affecting the acceleration of mass discharge in David glacier. Based on current knowledge, ice shelf buttressing effect, basal melting, and SMB (surface mass balance) are the components that have been known to affect glacier speed. Here, 2D Shallow Shelf Approximation model of the Ice Sheet System Model was used to predict response of glacier velocity distribution and contribution of sea level equivalent change depending on various forcing scenarios. Firstly, friction coefficient beneath glacier and ice rigidity on floating ice were estimated through inversion method, which constructed the initial condition of the regional model. Then, changing SMB, floating ice melting rate, and ice front position retreat could alter the sea level rise contribution and ice velocity. In the results, basal drag stress obtained through inversion method was largely calculated in the ice fall area where the subglacial ridge existed. Sea level equivalent for control model was -2.0 mm equivalent to ice mass gain of 15 Gt/yr during 50 years, and relatively stable than other fast flow regions, such as Pine Island Glacier. Ice front retreat over

threshold, which was about 90 km from ice front, accelerated the ice velocity near grounding line larger than twofold floating ice melting rate. This ice velocity acceleration influenced increase in sea level equivalent of -1.95 mm in case of furthermost ice front retreat. However, ice tongue and 8 km region of ice shelf position did not affect the ice velocity acceleration.

Key words : David Glacier, Sea level equivalent, Floating ice melting rate, Ice front position, Shallow Shelf Approximation model

TABLE OF CONTENTS

LIST OF FIGURES

LIST OF TALBES

1. INTRODUCTIONS

1.1. Background

According to 5th IPCC report, average global temperature of combined land and ocean was increased by 0.85 ℃ from 1880 to 2012, due to greenhouse gases (GHG) emitted by human activity. As global temperature was raised, mass loss of polar glacier and mountain glacier, which affected the sea-level rise(SLR) and submerged lower land, were in the spotlight. Potential Sea Level Rise for each reservoir is 58.3 m for Antarctica and 7.36 m for Greenland (Vaughan et al., 2013). Tuvalu, an island located in the Pacific ocean, was one of evidently submerged area due to SLR.

The Antarctica is comprised of West Antarctica ice sheet (WAIS) and East Antarctica ice sheet (EAIS), divided by the Transantarctic Mountains. An potential SLR for each region of Antarctica is 4.3 m for WAIS and 53.3 m for EAIS (Fretwell et al., 2013). Even though EAIS has a larger SLE than WAIS, previous studies have focused on the ice shelf loss of WAIS; where ice shelf provides buttress for ice sheet(DeConto and Pollard, 2016). After one of biggest ice shelf, Larsen B (3200 km^2), was collapsed in 2002, centerline velocity of four glacier was increased up to 2-6 times (Scambos et al., 2004). This ice shelf loss was not directly contributed to sea level rise, but it made the buttress of ice sheet weak and the ice discharge from ice sheet accelerated. Ice sheet mass loss of Antarctica increased from 30 Gt/year (1992-2001) to 147 Gt/year (2002-2011) (Vaughan et al., 2013) and acceleration for ice sheet mass loss was 14.5$\pm$2 Gt/year^2 for 18 years (1992-2010) (Rignot et al., 2011). Ice discharge of WAIS for 106$\pm$60 Gt/year in 2000 was larger than EAIS for -4$\pm$61 Gt/year (Rignot et al., 2008), which was relatively stable around 14 million

years ago (Barrett, 2013).

As it is important to evaluate the future SLR and evaluate glacial behavior, depending on future climate forcing, many models have been developed: Full Stokes model, Higher Order model, and Shallow Shelf Approximation model. A Full Stokes (FS) equation is the best tool for explaining the glacier dynamics. However, computation cost of FS is so high that other models have been developed, such as Higher Order model (3D model) and Shallow Shelf Approximation model (2D model). HO and SSA have some assumptions for simplifying momentum equation, so that HO and SSA have an error in predicting future sea level rise. For example, SSA overestimated SLR by 40%, compared with FS(Pattyn and Durand, 2013). Although SSA had limitation in future prediction, its computational efficiency compared to HO and FS enable various experiments (Morlighem et al., 2016; Schlegel et al., 2015).

To perform the regional model, it was important to estimate ice property parameters, such as basal friction coefficient on ice sheet and ice rigidity on ice shelf. These parameters was hardly measured directly so inversion method, which facilitated estimation of parameters indirectly, was developed (MacAyeal, 1989; Morlighem et al., 2010; Morlighem et al., 2013). Parameters from inversion method established the initial parameters of transient simulation.

When grounding line position, which divided the region of ice shelf (floating ice) and ice sheet (grounded ice), was retreated to inland, it was hard for grounding line of marine ice sheet to be returned to the original condition (Schoof, 2007). This situation is called as marine ice sheet instability (MISI), Marine ice sheet is defined as the bed elevation of ice sheet under the sea level. The retreat of grounding line steepened horizontal thickness gradient which accelerated the ice sheet(Rignot and

Jacobs, 2002). To identify whether ice sheet is prone to MISI, several forcing variables experiments had been conducted, such as snow mass balance (SMB), size of mesh, floating ice melting rate, ice front position (Favier et al., 2014; Seroussi et al., 2014b) and geothermal heat flux (Pittard et al., 2016). One of influential factors affecting the ice discharge was floating ice melting rate and ice front retreat(Favier et al., 2014; Seroussi et al., 2014b).

1.2. David Glacier

Antarctica was the south polar ice sheet that restored the largest fresh water in an ice form. It would affect the SLR, as its mass loss was increased. EAIS relatively gained near zero mass balance of -4 ± 61 Gt/yr, compared to West Antarctica, which was the largest ice loss region of Antarctica(Rignot et al., 2008).

Victoria Land David Glacier (DAG), which included Dome C and Talos and was largest ice glacier of Northern Victoria Land, about 264,000 km^3 (Rignot et al., 2011) (Figure 1.(b)). An interior ice sheet was drained into Terra Nova Bay through Drygalski Ice Tongue (DIT) (Wuite et al., 2009), which had an important role on production and size of Terra Nova Bay polynya (Frezzotti and Mabin, 1994). Before DAG was directly connected to DIT, ice velocity was distorted by fjord-like valley, and subglacial ridge was located at icefall (Rignot, 2002). Average thickness along grounding line was estimated by values of 1900 ± 200 m with Interferometric Synthetic Aperture Radar (InSAR), however, its value was not reliable, compared to grounding penetrating radar(GPR). The direct measurement of ice thickness at grounding line was 2530 m reported by Swithinbank (1988). A mass balance of DAG was relatively zero of -3 ± 6 Gt/yr (Rignot et al., 2008).

Velocity of David Glacier was not changed dramatically during 1991 to 2000 (Wuite et al., 2009). A calving events lost large area of DIT hit by iceberg B15A and C16 in 2005 and 2006 (Wuite et al., 2009) and several calving events occurred before 20th century.

In Figure 1(b), purple line indicates cross section line ($\overline{AA`}$), and white line was grounding line position. Domain outline in Figure 1(b) was referred from drainage system of Rignot et al. (2008). Bed geometry had retrograding slope at the

grounding line, however, the bed elevation of inland glacier is higher than bed elevation on ice shelf (Figure 2).

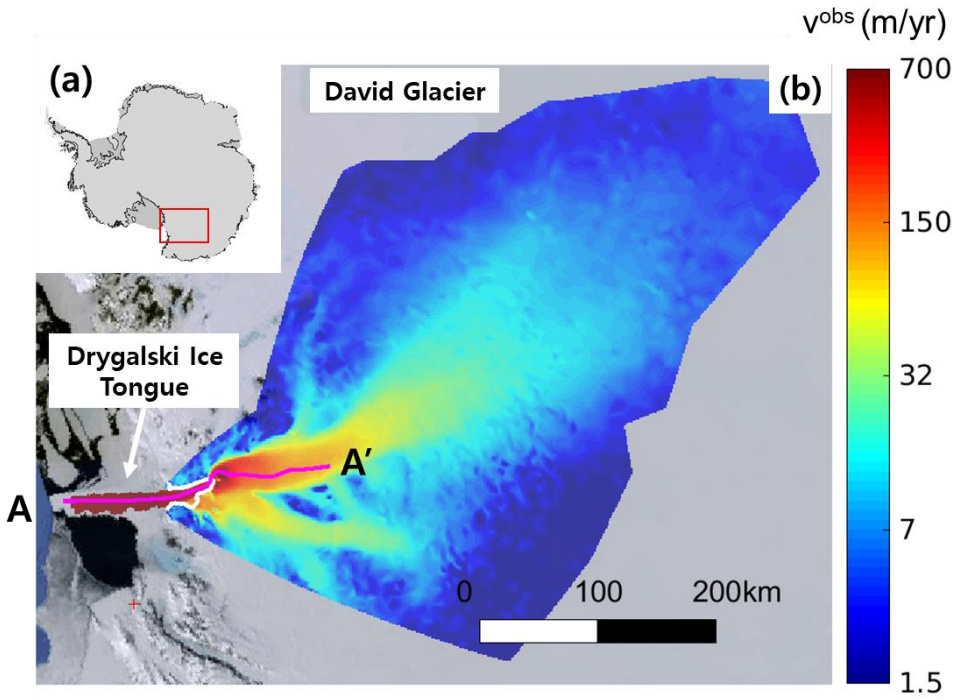

Figure 1. Location of David Glacier (DAG), Drygalski Ice Tongue(DIT). (a) shows the whole domain of Antarctica, where black line represents grounding line and red box indicates David Glacier region. (b) shows location of Drygalski Ice Tongue (DIT) at David Glacier (DAG) overlain observed surface ice velocity mainly covered during 2007 to 2009, as well as between 2013 and 2016 (Mouginot et al., 2012). In illustration (b), purple line (AA') represents a flow line for Figure 2, and white line is grounding line.

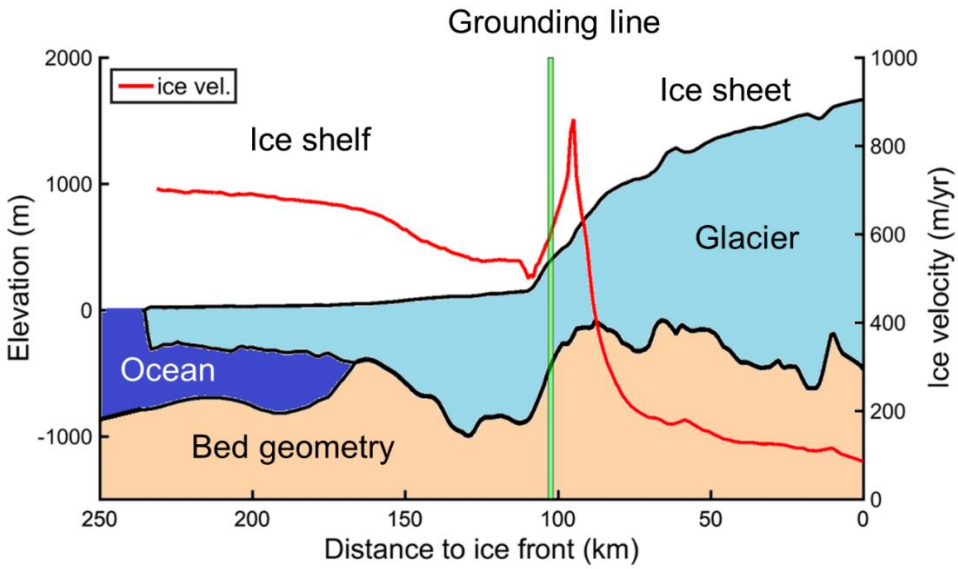

Figure 2. Cross section of Drygalski Ice Tongue along cross section line($\overline{AA`}$) shown in Figure 2.(b). Ice velocity is indicated as red line, and grounding line is green box at about 130 km from ice front.

1.3. Objectives

Currently, investigation for basal friction, internal temperature, ice rigidity of global/regional scale was performed. Main interest of previous studies was initialization of model and access to understanding glacier internal dynamics. Also, various climate forcing scenarios were envisaged, and applied to initial condition of model for examining the change in glacier dynamics. For DAG, observation data and internal ice dynamic information had been constructed to some extent, however, it remained unclear whether DAG will continue to accelerate and how sea level contribution will be changed depending on various forcing scenarios. In this study, i) initial condition for regional scale model on DAG was constructed through the 2D SSA model with inversion method, and ii) ice velocity and sea level equivalent change were investigated though application of various climate forcing scenarios, such as change in SMB, floating ice melting rate, and ice front position retreat.

2. METHODS

Ice Sheet System Model(ISSM) developed by Jet Propulsion Laboratory, USA, and University of California at Irvine, USA, is open source software, which modeled ice dynamic model (Larour et al., 2005; Larour et al., 2012; Morlighem et al., 2010; Morlighem et al., 2013). This software is state-of-art model to solve stress equation and mass transport model based on finite element method (FEM). There three types of equation, Full Stokes model, Higher-Order model, and Shallow Shelf Approximation model (SSA). Here, SSA model, where gravitational driving force was balanced with basal friction and other adjustment of stress field, was applied to this study.

ISSM model solved partial differential equation with Continuous Galerkin Finite Element Method(FEM), which is useful method for solving discretization of the ice flow equation. Also, this method is efficient means to solve unstructured mesh, which allows to enhance computational cost. Mesh imposes triangular Lagrange P1 elements for 2D SSA model, prismatic P1 elements in 3D, except for FS.

In case of mass transport model, implicit finite difference approximation was more used. When Galerkin FEM was applied to solve hyperbolic partial differential equation, such as mass transport model, instability of model was introduced. However, implicit method was more stable than explicit scheme.

Various input data, which consisted of surface mass balance, surface elevation, bed elevation, ice thickness, floating ice melting rate, ice temperature, and ice velocity, were acquired for performing glacier dynamics models. These data were obtained from direct measurement, such as ice thickness and surface mass balance, or indirect means that ice velocity was estimated from satellite data. Additional glacial

parameters, such as friction coefficient beneath glacier and ice rigidity on ice shelf, were used to model glacial dynamics, and acquired indirectly by using inversion method.

2.1. Stress Balance Models

2.1.1. Full Stokes Model (FS)

Full stokes (FS) set of equation with momentum balance equation and incompressibility equation is more suitable for representing the ice flow model and is derived from Navier-Stokes equation(NS), where local acceleration is neglected. Momentum equation of FS is expressed as Eq. 1, where ice is assumed as isotropic and incompressible material.

$$\nabla \cdot \boldsymbol{\sigma} + \rho_{\mathrm{i}} \mathbf{g} = \mathbf{0} \qquad \text{Eq. 1}$$

$$\nabla \cdot \mathbf{u} = 0 \qquad \text{Eq. 2}$$

, where $\boldsymbol{\sigma}$ is stress tensor (Pa), $\nabla \cdot \boldsymbol{\sigma}$ is the divergence of the stress tensor, $\mathbf{g}$ is gravitational acceleration (m/s^2), ρ_i is density of ice (kg/m^3), and $\mathbf{u}$ (m/s) is velocity vector (u, v, w) for x,y, and z components in Cartesian coordinate. Momentum equation can be denoted by

$$\begin{pmatrix} \frac{\partial \sigma_{xx}}{\partial x} & \frac{\partial \sigma_{xy}}{\partial y} & \frac{\partial \sigma_{xz}}{\partial z} \\ \frac{\partial \sigma_{yx}}{\partial x} & \frac{\partial \sigma_{yy}}{\partial y} & \frac{\partial \sigma_{yz}}{\partial z} \\ \frac{\partial \sigma_{zx}}{\partial x} & \frac{\partial \sigma_{zy}}{\partial y} & \frac{\partial \sigma_{zz}}{\partial z} \end{pmatrix} = \begin{pmatrix} 0 \\ 0 \\ \rho_i g \end{pmatrix} \qquad \text{Eq. 3}$$

The deformation of ice under stress is explained by the material constitutive law. In case of incompressible viscous fluids, the constitutive law is

$$\sigma'_{i,j} = 2\mu \dot{\epsilon}_{i,j} \qquad \text{Eq. 4}$$

, where $\boldsymbol{\sigma}' = \boldsymbol{\sigma} - \frac{1}{3}\delta_{ij} \sum_k \boldsymbol{\tau}_{kk}$ is deviatoric stress tensor, δ_{ij} is Kronecker delta

$$\delta_{\mathrm{ij}} = \begin{cases} 1 & if \;\; i = j \\ 0 & if \;\; i \neq j \end{cases} \qquad \text{Eq. 5}$$

, μ is an effective viscosity (Pa s), and $\dot{\epsilon}_{i,j} = \frac{1}{2}\left(\frac{\partial u_i}{\partial x_j} + \frac{\partial u_j}{\partial x_i}\right)$ is a strain rate tensor.

The effective viscosity is assumed to be non-linear and follows Glen's law (Glen (1955)), which well describes the viscous flow of ice :

$$\mu = \frac{1}{2} B(\theta) \dot{\epsilon_e}^{(1-n)/n} \qquad \text{Eq. 6}$$

, where $\dot{\epsilon}_e^2 = \frac{1}{2}\sum_{i,j} \dot{\epsilon}_{i,j}\dot{\epsilon}_{i,j}$ is the square of the second invariant of the strain rate tensor. n =3 is the Glen's flow law exponent in model, B(θ) is ice rigidity (Pa $a^{1/n}$) dependent on a temperature field, and θ is an ice temperature (K).

Eq. 3 can be expressed in the velocity term and pressure with substituting deviatoric stress by;

$$\begin{pmatrix} \frac{\partial}{\partial x}\left(2\mu\frac{\partial u}{\partial x}\right) & \frac{\partial}{\partial y}\left(\mu\frac{\partial v}{\partial x}+\mu\frac{\partial u}{\partial y}\right) & \frac{\partial}{\partial z}\left(\mu\frac{\partial w}{\partial x}+\mu\frac{\partial u}{\partial z}\right) \\ \frac{\partial}{\partial x}\left(\mu\frac{\partial v}{\partial x}+\mu\frac{\partial u}{\partial y}\right) & \frac{\partial}{\partial y}\left(2\mu\frac{\partial v}{\partial y}\right) & \frac{\partial}{\partial z}\left(\mu\frac{\partial w}{\partial y}+\mu\frac{\partial v}{\partial z}\right) \\ \frac{\partial}{\partial x}\left(\mu\frac{\partial w}{\partial x}+\mu\frac{\partial u}{\partial z}\right) & \frac{\partial}{\partial y}\left(\mu\frac{\partial w}{\partial y}+\mu\frac{\partial v}{\partial z}\right) & \frac{\partial}{\partial z}\left(2\mu\frac{\partial w}{\partial z}\right) \end{pmatrix} = \begin{pmatrix} \frac{\partial P}{\partial x} \\ \frac{\partial P}{\partial y} \\ \rho_i g + \frac{\partial P}{\partial z} \end{pmatrix} \qquad \text{Eq. 7}$$

, where P is the ice pressure (Pa). Viscosity of ice depends on the temperature, so that thermal energy equation should be solved by

$$\rho\frac{\mathrm{d}(c_\rho\theta)}{dt} = \nabla(k_i\nabla\theta) + \Phi_i \qquad \text{Eq. 8}$$

, where θ is the ice temperature (K), c_p is heat capacity of ice with value of 2093 J kg^{-1} K^{-1}, k_i is thermal conductivity of ice with value of 0.24 W m^{-1} K^{-1}, Φ_i is internal frictional heating due to ice deformation (W m^{-3}) (Larour et al., 2012; Pattyn, 2003).

2.1.2. Higher Order Model (HO)

FS has so high computation cost that Pattyn (2003) suggested Higher Order model derived from FS, using balance laws of mass, momentum and energy, extended with a constitutive equation. HO method assumed that (a) horizontal gradient of vertical velocity and (b) neglecting bridging (Van Der Veen and Whillans, 1989), where cavity (or hallow) cannot support the ice mass so that the stress is transferred to the near area, can be neglected. First assumption can be expressed as;

$$\dot{\epsilon}_{xz} = \frac{1}{2}\frac{\partial u}{\partial z}, \qquad \dot{\epsilon}_{yz} = \frac{1}{2}\frac{\partial v}{\partial z} \qquad \text{Eq. 9}$$

, where $\frac{\partial w}{\partial x}$ and $\frac{\partial w}{\partial y}$ was zero. Second assumption can be written as (Van Der Veen and Whillans, 1989), and third term of Eq. 7 can be reduced to

$$\frac{\partial}{\partial z}\left(2\mu\frac{\partial w}{\partial z}\right) = \rho_i g + \frac{\partial P}{\partial z} \qquad \text{Eq. 10}$$

The first and second term of FS equation (Eq. 7) are reduced to :

$$\frac{\partial}{\partial x}\left(4\eta\frac{\partial u}{\partial x} + 2\eta\frac{\partial v}{\partial y}\right) + \frac{\partial}{\partial y}\left(\eta\frac{\partial u}{\partial y} + \eta\frac{\partial v}{\partial x}\right) + \frac{\partial}{\partial z}\left(\mu\frac{\partial u}{\partial z}\right) = \rho_i g\frac{\partial s}{\partial x} \qquad \text{Eq. 11}$$

$$\frac{\partial}{\partial x}\left(\eta\frac{\partial u}{\partial y} + \eta\frac{\partial v}{\partial x}\right) + \frac{\partial}{\partial x}\left(4\eta\frac{\partial v}{\partial y} + 2\eta\frac{\partial u}{\partial x}\right) + \frac{\partial}{\partial z}\left(\mu\frac{\partial v}{\partial z}\right) = \rho_i g\frac{\partial s}{\partial v} \qquad \text{Eq. 12}$$

Eq. 11 and Eq. 12 are the core equations of HO model, which has only two components (u and v).

2.1.3. Shallow Shelf Approximation Model (SSA)

Shallow Shelf Approximation model (SSA) is the simplest model for explaining ice shelf region. SSA assumed that vertical shear stress is negligible (MacAyeal, 1989) :

$$\dot{\epsilon}_{xz} = \dot{\epsilon}_{yz} = 0 \qquad \text{Eq. 13}$$

, which of equation reduces 3D model to 2D and its horizontal velocity is not dependent on depth. Basal velocity is same as surface ice velocity. SSA model equation could be derived from Eq. 7 with Eq. 13 as follow :

$$\frac{\partial}{\partial x}\left(2\bar{\mu}H\left(2\frac{\partial u}{\partial x}+\frac{\partial v}{\partial y}\right)\right)+\frac{\partial}{\partial y}\left(\bar{\mu}H\left(\frac{\partial u}{\partial y}+\frac{\partial v}{\partial x}\right)\right)-\rho gH\frac{\partial s}{\partial x}=0 \qquad \text{Eq. 14}$$

$$\frac{\partial}{\partial y}\left(2\bar{\mu}H\left(2\frac{\partial v}{\partial y}+\frac{\partial u}{\partial x}\right)\right)+\frac{\partial}{\partial x}\left(\bar{\mu}H\left(\frac{\partial u}{\partial y}+\frac{\partial v}{\partial x}\right)\right)-\rho gH\frac{\partial s}{\partial y}=0 \qquad \text{Eq. 15}$$

, where $\bar{\mu}$ was depth averaged ice viscosity, and H is ice thickness. Here, the SSA model is chosen for study area.

2.1.4. Boundary Conditions

Following the Morlighem et al. (2013), ice boundary condition, $\partial\Omega$, for FS, HO, and SSA consisted with three interfaces, such as atmosphere(Γ_s), bedrock(Γ_b), and ocean(Γ_w), which can be written as;

$$\partial\Omega = \Gamma_s \cup \Gamma_w \cup \Gamma_b \qquad \text{Eq. 16}$$

For FS, boundary condition is defined by

$$\boldsymbol{\sigma} \cdot \mathbf{n} = \mathbf{0} \quad \text{on} \quad \Gamma_s \qquad \text{Eq. 17}$$

$$(\boldsymbol{\sigma} \cdot \boldsymbol{n} \cdot \boldsymbol{n} + \alpha^2 \boldsymbol{v}) = 0 \quad \text{on} \quad \Gamma_b \qquad \text{Eq. 18}$$

$$\mathbf{v} \cdot \mathbf{n} = 0 \quad \text{on} \quad \Gamma_b$$

$$\boldsymbol{\sigma} \cdot \mathbf{n} = \rho_w g z \boldsymbol{n} \quad \text{on} \quad \Gamma_w \qquad \text{Eq. 19}$$

, where **n** is the normal vector and α is friction coefficient ($Pa^{1/2}$ $s^{1/2}$ $m^{1/2}$). Basal friction (Pa), $\boldsymbol{\tau}_b$, can be called as basal drag, basal traction, or basal shear stress, which is defined as

$$\boldsymbol{\tau}_b = -\alpha^2 \boldsymbol{v_b} \qquad \text{Eq. 20}$$

, where friction coefficient at ice shelf was assumed to be negligible, however. friction coefficient of ice sheet was guessed by inversion method, which will be described.

For HO, these boundary conditions for HO model referred from Morlighem et al. (2013) could rewritten as :

$$\begin{cases} 2\mu \boldsymbol{\epsilon'_x} \cdot \boldsymbol{n} = 0 \\ 2\mu \boldsymbol{\epsilon'_y} \cdot \boldsymbol{n} = 0 \end{cases} \quad \text{on} \quad \Gamma_s \qquad \text{Eq. 21}$$

$$\begin{cases} 2\mu \boldsymbol{\epsilon'_x} \cdot \boldsymbol{n} = -\alpha^2 v_x \\ 2\mu \boldsymbol{\epsilon'_y} \cdot \boldsymbol{n} = -\alpha^2 v_y \end{cases} \quad \text{on} \quad \Gamma_b \qquad \text{Eq. 22}$$

$$\begin{cases} 2\mu \boldsymbol{\epsilon'_x} \cdot \boldsymbol{n} = \rho g (s - z) n_x \\ 2\mu \boldsymbol{\epsilon'_y} \cdot \boldsymbol{n} = \rho g (s - z) n_y \end{cases} \quad \text{on} \quad \Gamma_w,\ z \geq 0 \qquad \text{Eq. 23}$$

$$\begin{cases} 2\mu\acute{\boldsymbol{\epsilon}}_{\boldsymbol{x}} \cdot \boldsymbol{n} = (\rho g(s-z) + \rho_w g z) n_x \\ 2\mu\acute{\boldsymbol{\epsilon}}_{\boldsymbol{y}} \cdot \boldsymbol{n} = (\rho g(s-z) + \rho_w g z) n_y \end{cases} \quad \text{on} \quad \Gamma_w, \text{ z<0}$$

, where $\acute{\boldsymbol{\epsilon}}_{\boldsymbol{x}} = (\epsilon_{xx}, \epsilon_{yx}, \epsilon_{zx})$ and $\acute{\boldsymbol{\epsilon}}_{\boldsymbol{y}} = (\epsilon_{xy}, \epsilon_{yy}, \epsilon_{zy})$.

For SSA, boundary conditions are;

$$\begin{cases} 2\bar{\mu}\acute{\boldsymbol{\epsilon}}_{\boldsymbol{x}} \cdot \boldsymbol{n} - \alpha^2 \bar{u} = \rho g H \dfrac{\partial s}{\partial x} \\ 2\bar{\mu}\acute{\boldsymbol{\epsilon}}_{\boldsymbol{y}} \cdot \boldsymbol{n} - \alpha^2 \bar{v} = \rho g H \dfrac{\partial s}{\partial y} \end{cases} \qquad \text{Eq. 24}$$

, where $\bar{\boldsymbol{v}} = (\bar{u}, \bar{v})$ is depth averaged velocity (m/s). For SSA model, driving force $\rho g H \nabla s$ is basically balanced with basal shaer stress.

2.1.5. Friction Coefficient Parameterization at Grounding Line

According to Seroussi et al. (2014a), method for estimating friction coefficient at grounding line controlled result of grounding line migration. Different simulation results were obtained depending on presence or absence parameterization of the basal friction coefficient (Seroussi et al., 2014a). In this study, sub-element parameterization method, which considers that friction coefficient is proportional to area of grounded ice of mesh element, was used to estimate the friction coefficient at grounding line(Figure 3).

$$\mathrm{C_g} = C\frac{A}{A_g} \qquad \text{Eq. 25}$$

, where C_g was an applied basal friction coefficient, A_g was area of grounded ice, A was area of element, and C is an inferred basal friction coefficient.

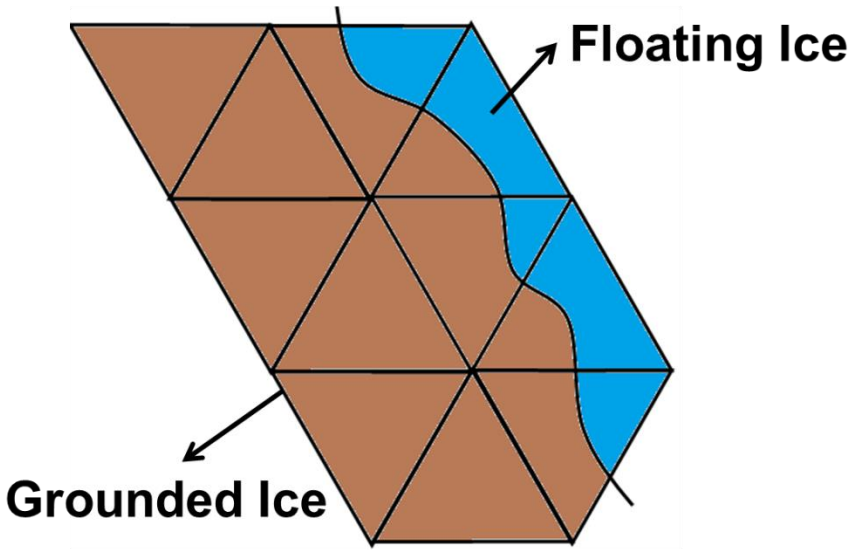

Figure 3. Friction coefficient parameterization at grounding line is proportional to grounded ice area.

2.2. Mass Transport Model

During transient simulation, surface mass balance and floating ice melting rate are introduced, and interacts with the ice flow through the mass transport model derived by mass conservation.

$$\frac{\partial \mathrm{H}}{\partial t} = -\nabla \cdot (H\overline{\boldsymbol{v}}) + \dot{M}_s + \dot{M}_b \qquad \text{Eq. 26}$$

,where $\bar{\mathbf{v}}$ = (u, v) is depth averaged velocity, $\dot{\mathrm{M}}_s$ is SMB (m/yr ice equivalent), and $\dot{\mathrm{M}}_b$ is floating ice melting rate (m/yr ice equivalent). Ice velocity is derived from ice flow model, such as SSA. The model doesn't include change in bed geometry and moving boundary condition. Surface velocity on domain could evolve freely during forward model. Here, it was assumed that the basal melting rate of ice shelf had depth dependent basal melting rate, method of which was introduced at Seroussi et al. (2014b) and (Favier et al., 2014).

2.3. Initialization

2.3.1. Input Data

Mesh

An initial mesh was generated with 1 km resolution mesh under the drainage system of DAG (Rignot et al., 2008). After that, initial mesh was adapted to the velocity field with 450 m gridded data, using Bidimensional Anisotropic Mesh Generator (BAMG) developed by Hecht (1998) (Figure 4). Mesh size was set as 1 km at grounding line and fast flow region and 10 km at internal ice sheet. The total number of elements is about 15,600, which was large enough to computing glacier model.

Surface velocity

Table 1 shows references of each input data. Ice velocity was estimated by using ALOS, TeraSAR-X, ENVISAT, ERS-1&2, RADARSAT-1&2, Sentinel-1, Landsat-8 satellites (Mouginot et al., 2012)(Figure 5). These satellites included antenna for transmitting radar pulses and receiving to create synthetic aperture radar (SAR). A phase difference can be calculated from different SAR image, which of investigation location were similar, and deformation of terrain was used for computing surface ice velocity.

SMB & Floating ice melting rate

Averaged SMB was from Arthern et al. (2006), where in situ measurements was combined with satellite observations of passive microwave (Figure 6), and it was constant in time. According to Wuite et al. (2009), the highest basal melting rate was

20.91±9.6 m/year near grounding line and the melting rate tended to decrease toward the ice front. From ice front with 80 km, base of ice shelf got a negative basal melting rate which meant that water was refreeze due to outlet of subglacial melting water (Massimo, 1993). Here, depth dependent parameterization was adopted to simulate floating ice melting rate. Deep water melting rate was 20 m/yr at -1200 m, and there was no melt at -300 m. Figure 7 displayed the distribution of floating ice melting rate, which of ice tongue rarely melted.

Ice temperature & Ice rigidity

For 2D model, it was necessary to calculate depth average viscosity from 3D thermal model, which required surface temperature and geothermal heat flux (Table 1). The Surface temperature was from Comiso (2000) (Figure 8), and the geothermal heat flux from Shapiro and Ritzwoller (2004), who estimated the geothermal heat flux with seismic model. Ice rigidity on ice shelf was estimated by inversion method that will be described in Section 2.3.2. below. The ice temperature on ice sheet from 3D thermal model was used for converting to ice rigidity by using temperature dependence of Cuffey and Paterson (2010) (Figure 9), and 2D ice rigidity was determined by vertically averaging 3D ice rigidity (Figure 10). The ice rigidity with the surface temperature of about -10℃ along coastal line is softer than internal ice sheet.

Table 1. This table shows datasets of source used in model.

Data	Name	References
Bed elevation	BedMachine	Morlighem et al.(2014)
Surface elevation	Bedmap2	Fretwell et al. (2013)
Surface velocity	MEaSUREs	Mouginot et al. (2012)
Surface mass balance	-	Arthern et al. (2006)
Air temperature	-	Comiso (2000)
Geothermal heat flux		Shapiro and Ritzwoller (2004)

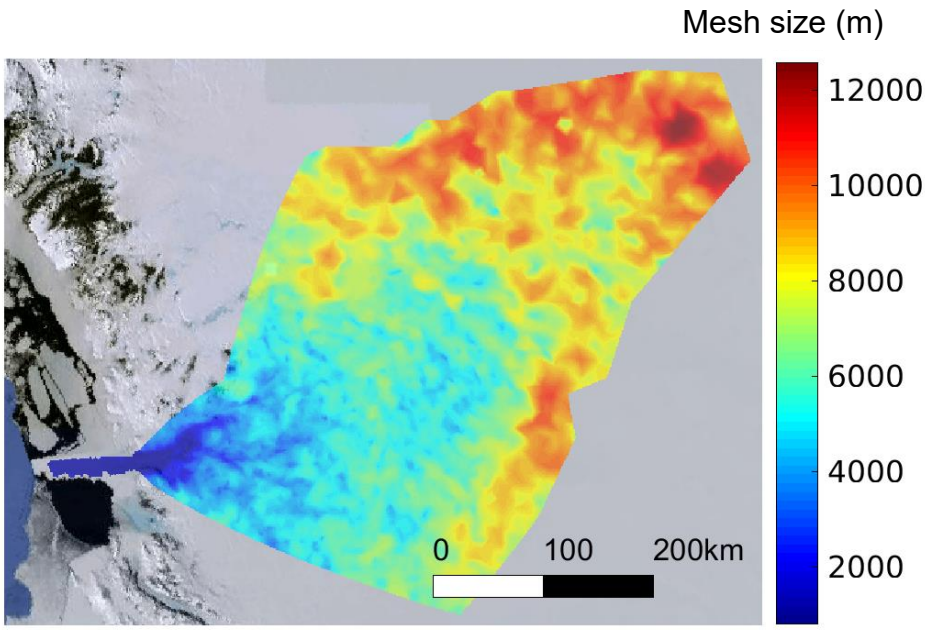

Figure 4. This figure shows a size of mesh used in model. A maximum mesh size at ice sheet is about 10 km and minimum mesh at ice shelf is about 1 km.

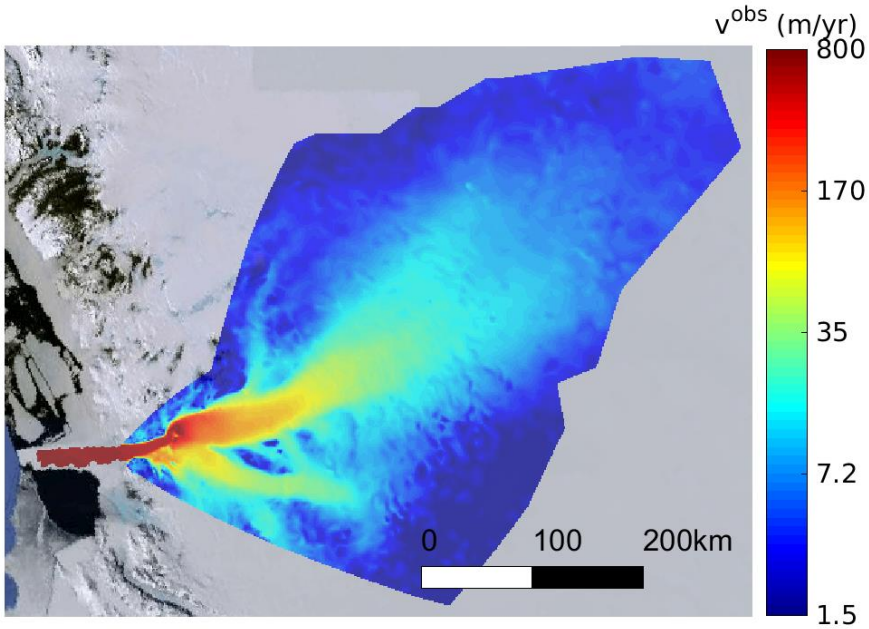

Figure 5. Spatial surface ice velocity distribution from Mouginot et al. (2012), who calculated the ice velocity, using InSAR with ALOS, TeraSAR-X, ENVISAT, ERS-1&2, RADARSAT-1&2, Sentinel-1/ESA, Landsat-8 satellites during 2007 to 2009, as well as between 2013 and 2016.

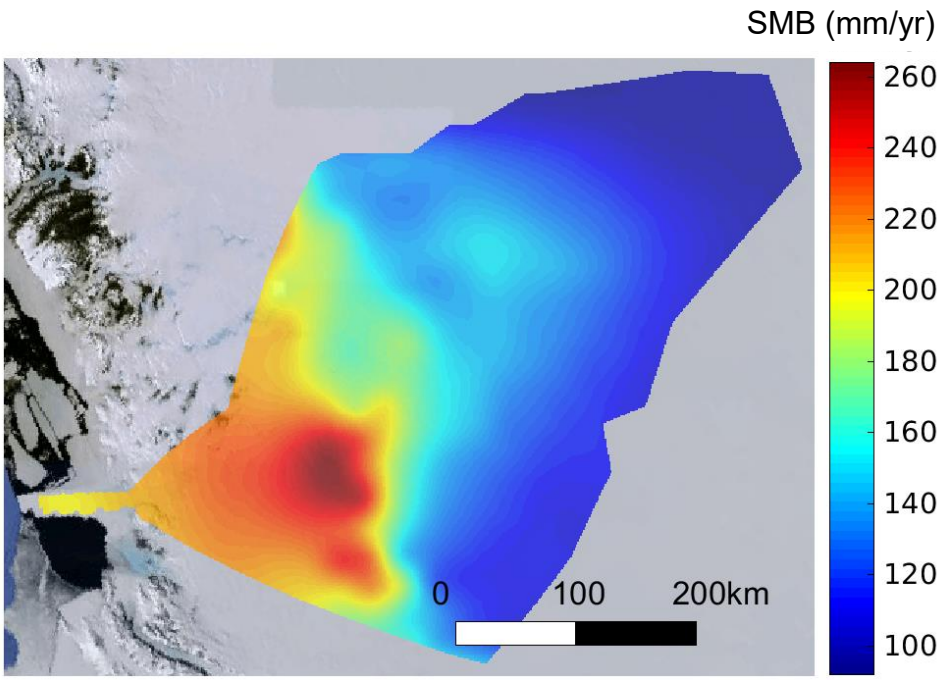

Figure 6. Surface mass balance (SMB) distribution from Arthern et al. (2006).

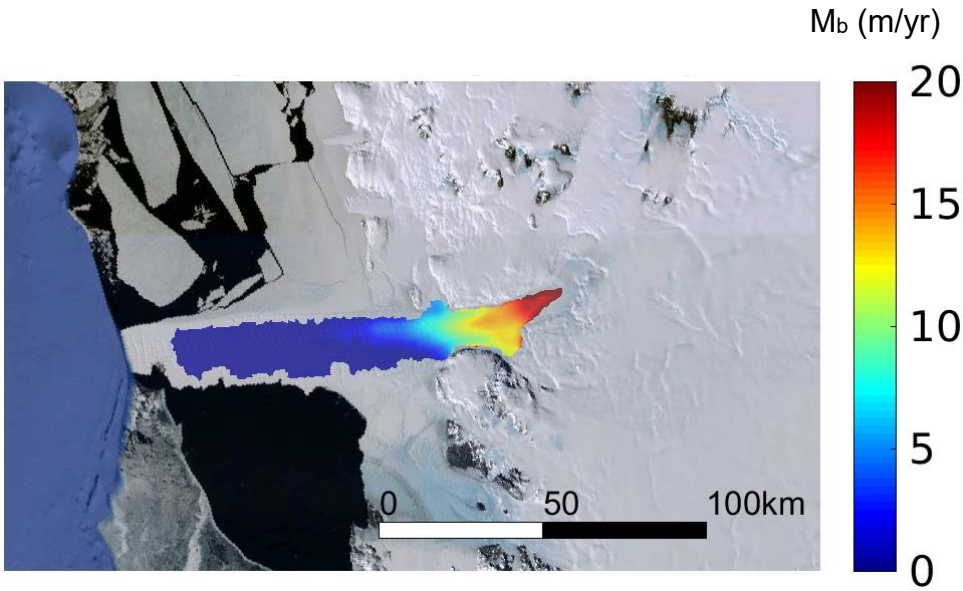

Figure 7. Floating ice melting rate distribution dependent on depth in respect to deep water melting with 20 m/yr at -1200 m and shallow water with zero melt at -300 m on ice shelf.

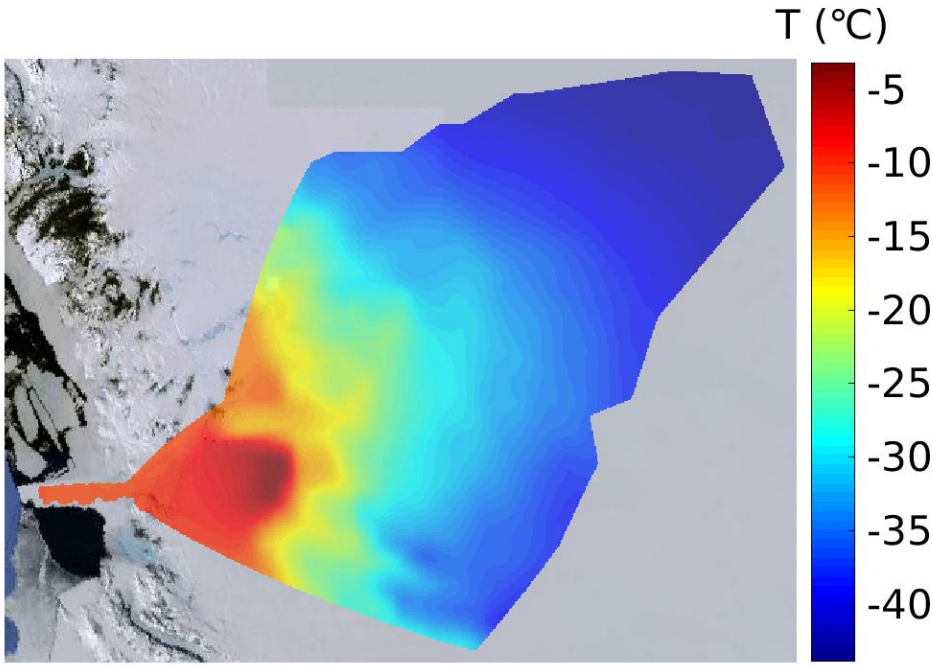

Figure 8. Air temperature distribution (Comiso, 2000).

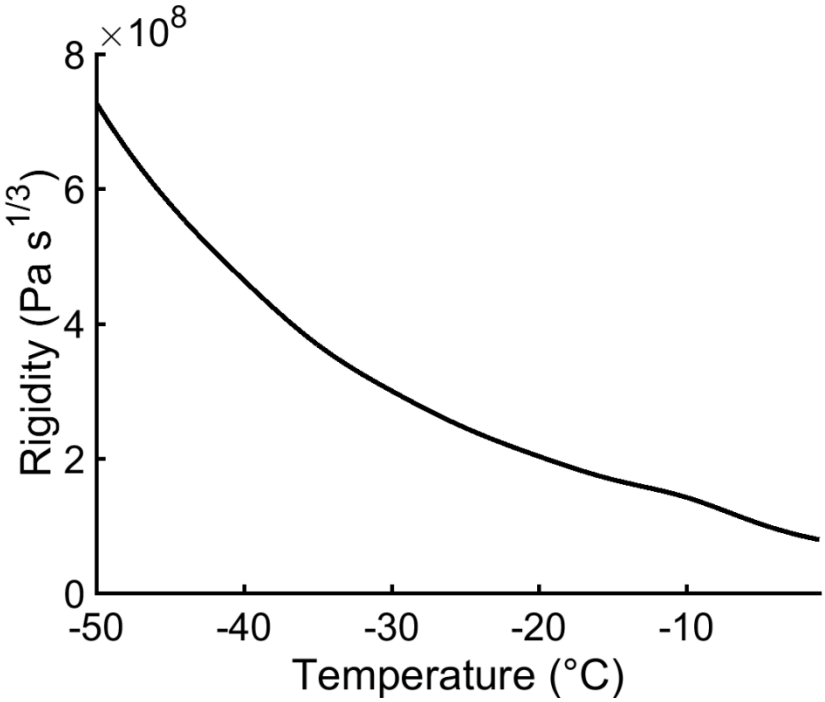

Figure 9. Temperature dependence of ice rigidity from Cuffey and Paterson (2010)

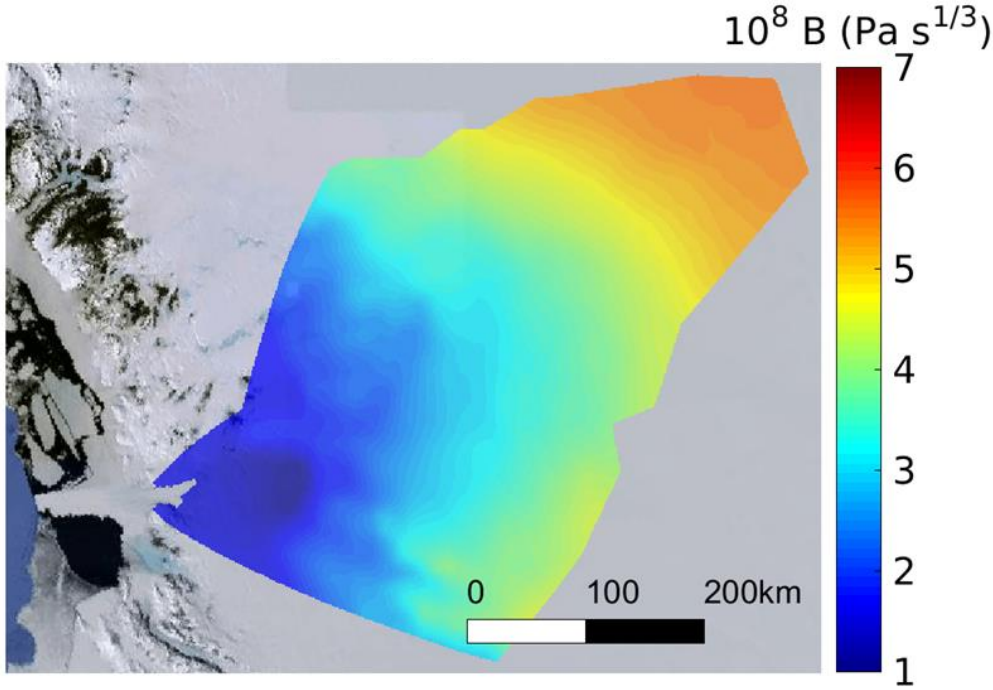

Figure 10. Ice rigidity on ice sheet from vertically averaging 3D ice rigidity, which is converted from 3D thermal model.

Geometry

Surface elevation data was extracted from Bedmap2 (Fretwell et al., 2013) (Figure 11). Bed elevation data, which of zero flux divergence was guaranteed on ice sheet, was used (Morlighem et al., 2014). If flux divergence was not ensured, the flux divergence affected the time evolution of the glacier, which was controlled by mass conservation. Flux divergence from mass transport model (Eq. 26) was written as :

$$-\nabla \cdot (H\overline{\boldsymbol{v}}) = -\overline{\boldsymbol{v}} \cdot \nabla H - H\nabla \cdot \overline{\boldsymbol{v}} \qquad \text{Eq. 27}$$

, where H is thickness of ice, and $\overline{\boldsymbol{v}}$ is depth averaged ice velocity. Depth averaged velocity from 3D model should be used for calculating the flux divergence, however, averages $||\overline{\boldsymbol{v}}||/||\boldsymbol{v}_s||$ on fast flow velocity, where ice velocity is >50 m/yr, were 99.0 % for HO and 98.9 % for FS (Seroussi et al., 2011). This result indicated that difference between surface ice velocity and depth averaged ice velocity was less than 1 %, therefore, surface ice velocity was used for depth averaged ice velocity. Figure 12 shows the flux divergence of Bedmap2 and Bedmachine data, where flight tracks for measuring thickness is indicated as black line. Anomalies of the flux divergence was introduced near grounding line, however, it was reduced after thickness data conserved mass and minimizes the observed thickness data. The flux divergence at ice fall showed still large values, which were > 50 m/yr. Figure 13 shows the bed elevation for (a) Bedmap2 and (b) Bedmachine. In Bedmap2, there is no bump near grounding line, however, reconstructing the bed elevation shows up the ice bumps clearly.

A base elevation at ice shelf was estimated by using hydrostatic equilibrium method, which showed a relationship between base elevation, b, and surface elevation, s. (Eq. 28).

$$\mathrm{b} = \mathrm{s}\frac{\rho_i}{\rho_i - \rho_w} \qquad \text{Eq. 28}$$

The base elevation at ice shelf was deeper than original bed elevation, so bed elevation was lowered with about 500 m for preventing readvance of grounding line(Figure 14).

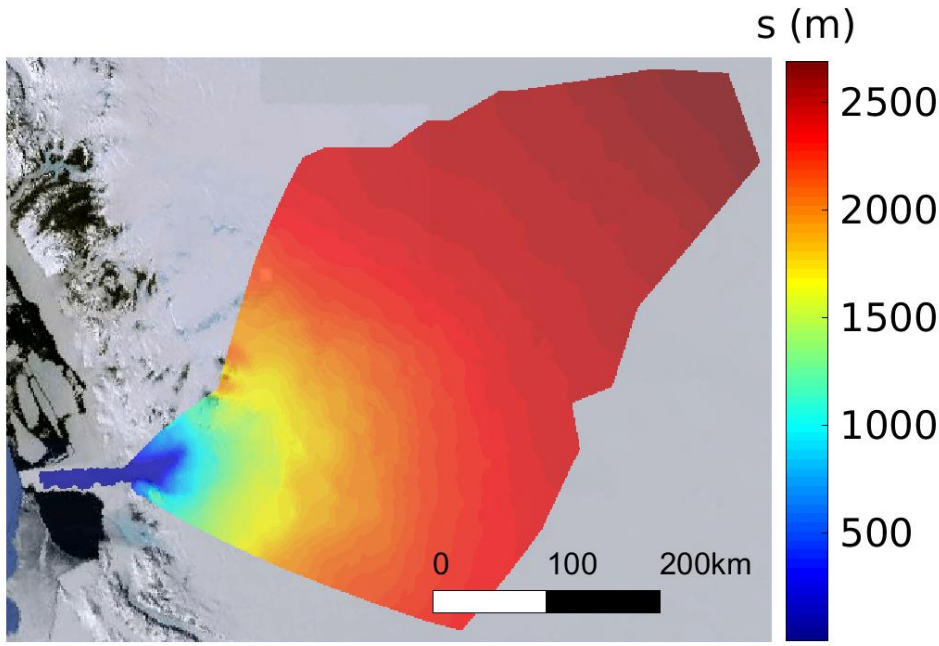

Figure 11. Surface elevation from Fretwell et al. (2013)

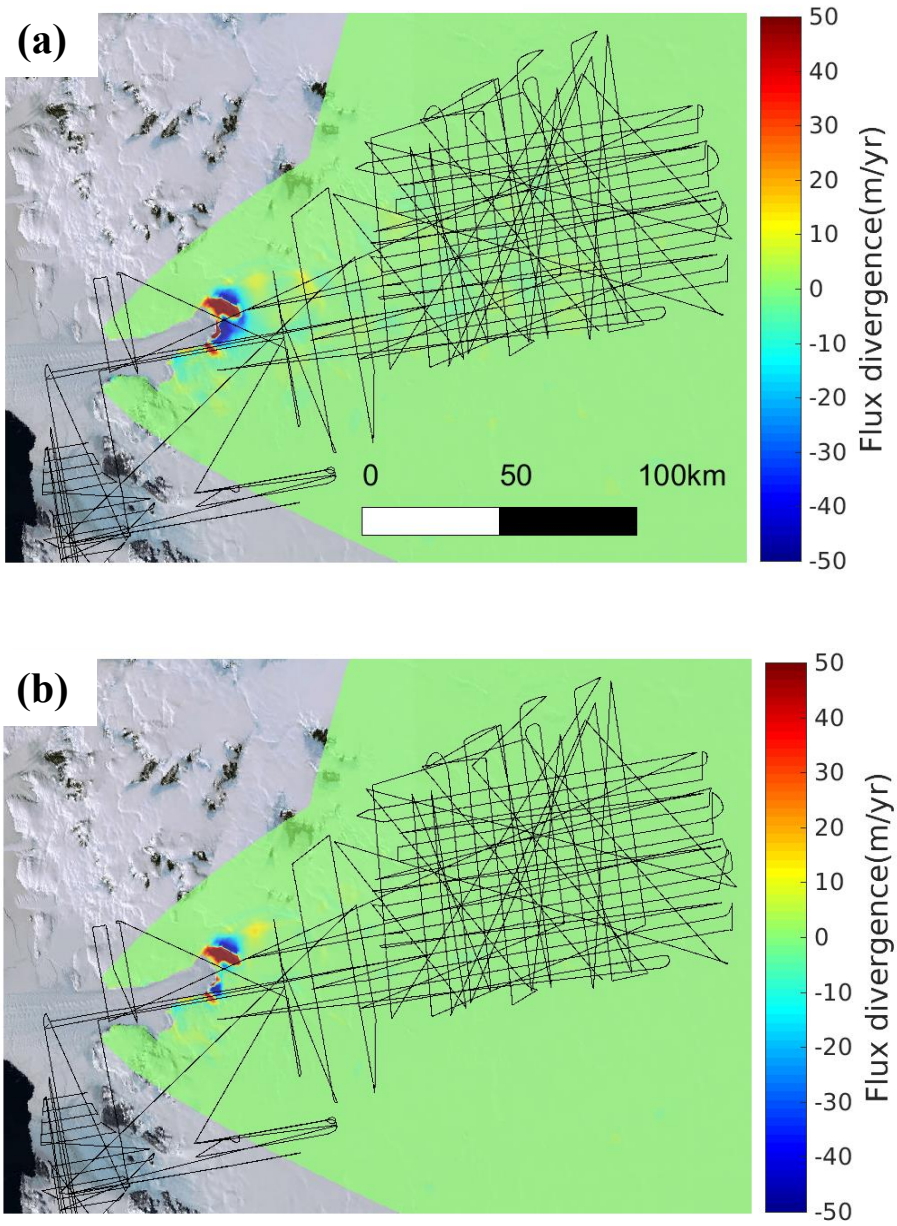

Figure 12. Flux divergence for (a) Bedmap2 (Fretwell et al., 2013) and (b) Bedmachine (Morlighem et al., 2014) data. Back line indicates additional flight tracks for measuring ice thickness used in Bedmachine.

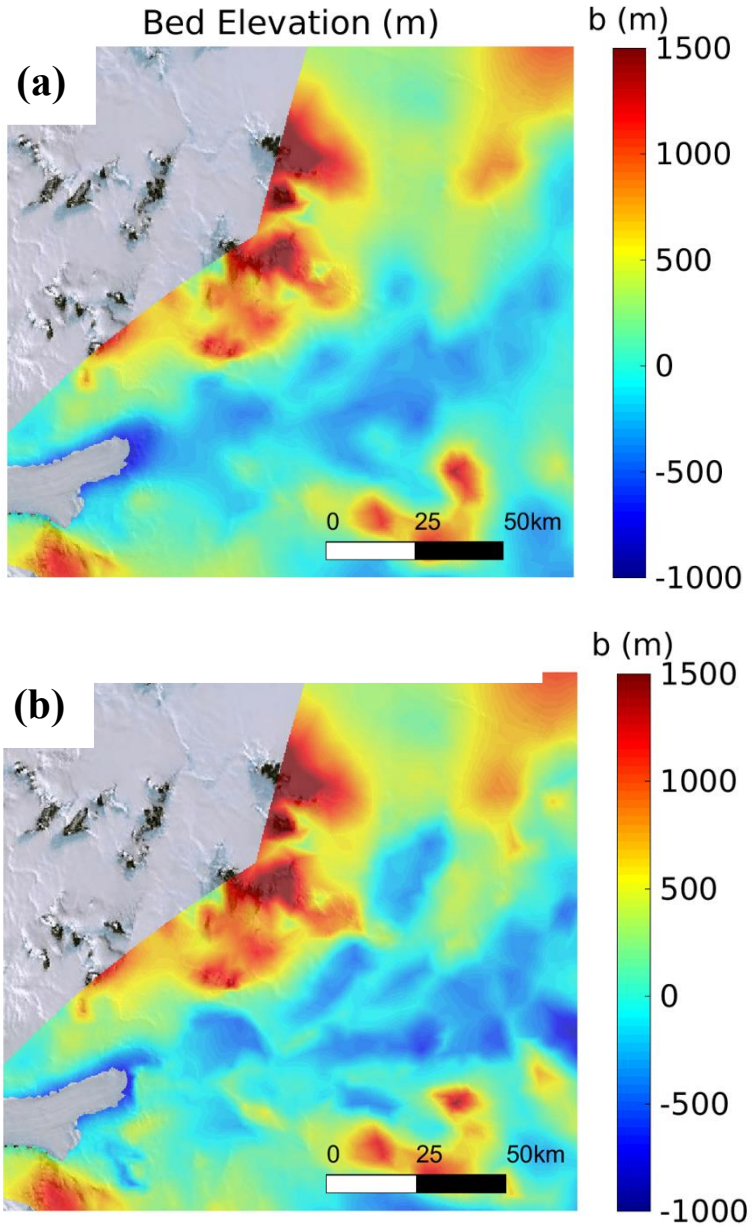

Figure 13. Bed elevation for (a) Bedmap2 (Fretwell et al., 2013) and (b) Bedmachine (Morlighem et al., 2014)

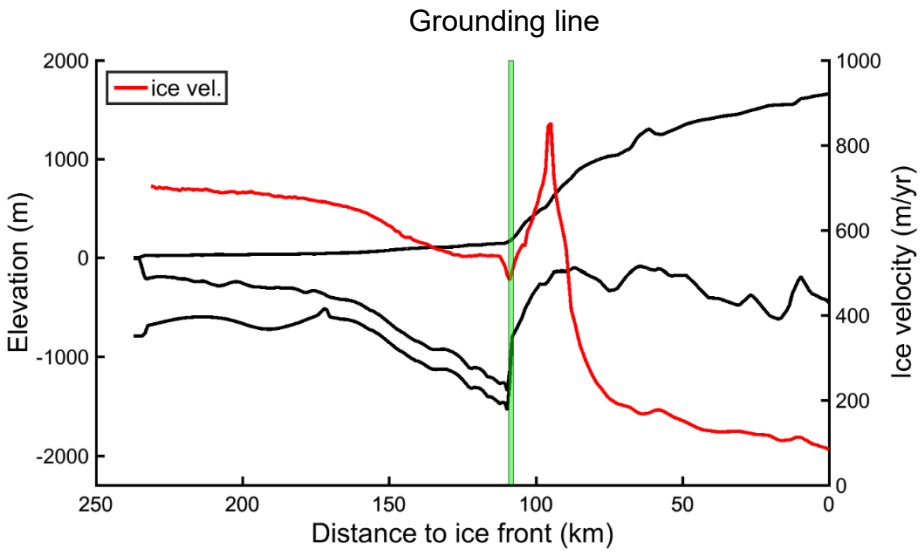

Figure 14. Profile for geometry and ice velocity along cross section line ($\overline{AA`}$, Figure 1(b)), where thickness of ice shelf satisfy with hydrostatic equilibrium and bed elevation at ice shelf is below 400 m from base elevation of ice shelf. Grounding line is located at 120 km from ice front (green line).

2.3.2. Basal Friction and Ice Rigidity

Before transient simulation model, it was important to estimate parameters of model, such as ice viscosity and friction coefficient. Various satellites and airborne data were used to obtain surface velocity, bed elevation, air temperature data, however, the basal friction coefficient under the glacial base was not directly measured. For estimation of friction coefficient, Eq. 14, Eq. 15, and Eq. 24 for SSA model could be written as below

$$\alpha = \frac{1}{\sqrt{u_d}}\left[\frac{\partial}{\partial x}\left(2\mu H\left(2\frac{\partial u}{\partial x}+\frac{\partial v}{\partial y}\right)\right)+\frac{\partial}{\partial y}\left(\mu H\left(\frac{\partial u}{\partial y}+\frac{\partial v}{\partial x}\right)\right) - \rho g H\frac{\partial s}{\partial x}\right]^{1/2} \quad \text{Eq. 29}$$

$$\alpha = \frac{1}{\sqrt{v_d}}\left[\frac{\partial}{\partial y}\left(2\mu H\left(2\frac{\partial v}{\partial y}+\frac{\partial u}{\partial x}\right)\right)+\frac{\partial}{\partial x}\left(\mu H\left(\frac{\partial u}{\partial y}+\frac{\partial v}{\partial x}\right)\right) - \rho g H\frac{\partial s}{\partial y}\right]^{1/2} \quad \text{Eq. 30}$$

, where (u_d, v_d) is basal velocity of ice. However, determination of friction coefficient may not be possible following reasons (MacAyeal, 1993). Frist, square root expression of Eq. 29 and Eq. 30 could become complexed values by velocity error. Secondly, zero velocity at some region introduce substitute denominator of righthand sides of Eq. 29 and Eq. 30, and β takes infinity. Thirdly, velocity error introduces oscillation in velocity derivatives. Here, we used inversion method for searching initial parameters of glacier flow model. The basal friction coefficient was inferred by using inversion method, called as control model, inversion model (Morlighem et al., 2010). The inversion method minimized a cost function, $J(\mathbf{v})$, which could be expressed as

$$J(\mathbf{v}) = w_1 \int_\Omega \frac{1}{2}((u-u_{obs})^2 + (v-v_{obs})^2)\, d\Omega$$

$$+ w_2 \int_\Omega \left(\log\left(\frac{\sqrt{u^2+v^2}+\epsilon}{\sqrt{u_{obs}^2+v_{obs}^2}+\epsilon} \right) \right) d\Omega \qquad \text{Eq. 31}$$

$$+ w_3 \int_\Omega \frac{1}{2} \nabla\alpha \cdot \nabla\alpha \, d\Omega$$

, where $\mathbf{v} = (u, v)$ is modeled velocity surface estimated through the inferred basal friction, $\mathbf{v}_{\boldsymbol{obs}} = (u_{obs}, v_{obs})$ is observed velocity, ϵ is a minimum velocity to avoid the observed velocity as zero, log is the natural logarithm, w_i is weight coefficient for each term. First equation, absolute misfit, works well at the high velocity field rather than low velocity, therefore, the logarithmic misfit, second term, is applied. However, this cost function is robust for basal drag coefficient, so that a Tikhonov regularization term, which penalizes an oscillation of basal friction coefficient, is applied to stabilize the control method(Morlighem et al., 2010). If rheology parameter is needed to determine, similar Eq. 31 can be applied with altering the parameter from the basal friction to rheology of ice.

The gradient of Eq. 31 is essential to find minimum cost function. Here, Lagrange multiplier is used to calculate the cost function. Each cost function weight is set up as w_1 = 1 and $w_2 = w_3$ =0 for describing the cost function simply (Morlighem et al., 2013). The Lagrangian, L, is

$$J(\mathbf{v}, \lambda, \alpha) = \frac{1}{2} \int_{\Gamma_s} \left(v_x - v_x^{obs}\right)^2 + \left(v_y - v_y^{obs}\right)^2 d\Gamma_s$$

$$+ \int_\Omega \lambda_x \left(\nabla \cdot (2\mu \dot{\boldsymbol{\epsilon}}_1) - \rho g \frac{\partial s}{\partial x} \right) d\Omega \qquad \text{Eq. 32}$$

$$+ \int_\Omega \lambda_y \left(\nabla \cdot (2\mu \dot{\boldsymbol{\epsilon}}_2) - \rho g \frac{\partial s}{\partial y} \right) d\Omega$$

, where $\boldsymbol{\lambda} = (\lambda_x, \lambda_y)$ are Lagrange multipliers, $\dot{\boldsymbol{\epsilon}}_1 = (2\frac{\partial u}{\partial x} + \frac{\partial v}{\partial y}, \frac{1}{2}\left(\frac{\partial u}{\partial y} + \frac{\partial v}{\partial x}\right))$ and $\dot{\boldsymbol{\epsilon}}_2 = (\frac{1}{2}\left(\frac{\partial u}{\partial y} + \frac{\partial v}{\partial x}\right), \frac{\partial u}{\partial x} + 2\frac{\partial v}{\partial y},)$. Second and third term at right hand side of this equation is integrated by parts, it can be rewritten as;

$$
\begin{aligned}
J(\mathbf{v}, \lambda, \alpha) = \frac{1}{2}\int_{\Gamma_s} \left(v_x - v_x^{obs}\right)^2 + \left(v_y - v_y^{obs}\right)^2 d\Gamma_s \\
- \int_{\Omega} (2\mu\dot{\boldsymbol{\epsilon}}_1) \cdot \nabla\lambda_x \; d\Omega - \int_{\Omega} (2\mu\dot{\boldsymbol{\epsilon}}_2) \cdot \nabla\lambda_y \; d\Omega \\
- \int_{\Omega} \rho g \nabla s \cdot \boldsymbol{\lambda} \; d\Omega - \int_{\Gamma_b} \alpha^2 \; \boldsymbol{v} \cdot \boldsymbol{\lambda} \; d\Gamma \\
+ \int_{\Gamma_b} \rho g s + (\rho_w - \rho) g z \; \boldsymbol{n} \cdot \boldsymbol{\lambda} \; d\Gamma
\end{aligned}
\qquad \text{Eq. 33}
$$

, where internal ice stress is balanced with friction and water pressure, which are valid at basal boundary (Γ_b) and ice front (Γ_w). Second and third term of Eq. 33 are integrated once again;

$$
\begin{aligned}
J(\mathbf{v}, \lambda, \alpha) = \frac{1}{2}\int_{\Gamma_s} \left(v_x - v_x^{obs}\right)^2 + \left(v_y - v_y^{obs}\right)^2 d\Gamma_s \\
+ \int_{\Omega} v_x \nabla \cdot \left(2\mu\dot{\boldsymbol{\epsilon}}_1(\lambda)\right) \; d\Omega \\
+ \int_{\Omega} v_y \nabla \cdot \left(2\mu\dot{\boldsymbol{\epsilon}}_2(\boldsymbol{\lambda})\right) \; d\Omega - \int_{\partial\Omega} v_x \; 2\mu\dot{\boldsymbol{\epsilon}}_1(\boldsymbol{\lambda}) \; d\Omega \\
- \int_{\partial\Omega} v_y \; 2\mu\dot{\boldsymbol{\epsilon}}_2(\boldsymbol{\lambda}) \; d\Omega - \int_{\Omega} \rho g \nabla s \cdot \boldsymbol{\lambda} \; d\Omega \\
- \int_{\Gamma_b} \alpha^2 \boldsymbol{v} \cdot \boldsymbol{\lambda} \; d\Gamma \\
+ \int_{\Gamma_b} \rho g s + (\rho_w - \rho) g z \; \boldsymbol{n} \cdot \boldsymbol{\lambda} \; d\Gamma
\end{aligned}
\qquad \text{Eq. 34}
$$

, where $\dot{\boldsymbol{\epsilon}}_{\mathbf{1}}(\boldsymbol{\lambda})$ and $\dot{\boldsymbol{\epsilon}}_{\mathbf{2}}(\boldsymbol{\lambda})$ are defined as:

$$\dot{\boldsymbol{\epsilon}}_{\mathbf{1}}(\boldsymbol{\lambda}) = \begin{pmatrix} 2\dfrac{\partial \lambda_x}{\partial x} + \dfrac{\partial \lambda_y}{\partial y} \\ \dfrac{1}{2}\left(\dfrac{\partial \lambda_y}{\partial x} + \dfrac{\partial \lambda_x}{\partial y}\right) \end{pmatrix} \quad \dot{\boldsymbol{\epsilon}}_{\mathbf{2}}(\boldsymbol{\lambda}) = \begin{pmatrix} \dfrac{1}{2}\left(\dfrac{\partial \lambda_y}{\partial x} + \dfrac{\partial \lambda_x}{\partial y}\right) \\ \dfrac{\partial \lambda_x}{\partial x} + 2\dfrac{\partial \lambda_y}{\partial y} \end{pmatrix} \qquad \text{Eq. 35}$$

Gâteaux derivative is used to derive the gradient cost function with basal friction coefficient, and it could be defined as with $^{\forall}\delta\alpha \subset \mathrm{H}^1(\Omega)$:

$$DJ(\alpha;\delta\alpha) = \lim_{\epsilon \to 0} \frac{J(\alpha+\delta\alpha) - J(\alpha)}{\epsilon} \qquad \text{Eq. 36}$$

, where $\mathrm{H}^1(\Omega)$ is Hilbert Space. The derivation of Lagrangian equation Eq. 34 is expressed with respect to basal friction coefficient, and Gâteaux derivative and chain rule are applied to it :

$$DJ(\alpha;\delta\alpha) = D_{\boldsymbol{v}}L\big(\boldsymbol{v}; D_\alpha(\boldsymbol{v};\delta\alpha)\big) + D_\lambda L\big(\boldsymbol{\lambda}; D_\alpha(\boldsymbol{\lambda};\delta\alpha)\big) + D_\alpha L(\boldsymbol{v};\delta\alpha) \qquad \text{Eq. 37}$$

If $\boldsymbol{v}$ is solution of Lagrangian equation(Eq. 34) and λ is chosen for making derivative of Lagrangian equation with respect to model state disappearing, Eq. 37 becomes

$$DJ(\alpha;\delta\alpha) = D_\alpha L(\boldsymbol{v};\delta\alpha) = -\int_{\Gamma_b} 2\alpha \;\; \delta\alpha \;\; \boldsymbol{v}\cdot\boldsymbol{\lambda} \;\; d\Gamma \qquad \text{Eq. 38}$$

This equation is easy to make cost function minimum value. In case of steepest descent algorithm for finding new basal friction coefficient, it is the fastest way to minimize the cost function with parallel diction of derivative of cost function.

$$\alpha_{new} = \alpha_{old} - \beta \frac{DJ(\alpha;\delta\alpha)}{||DJ(\alpha;\delta\alpha)||} \qquad \text{Eq. 39}$$

, where β is positive scalar coefficient, and α_{new} and α_{old} are updated and previous basal friction coefficient. To find the gradient of cost function, it is necessary to choose λ with

$$D_v J(\mathrm{v}, \lambda; \delta\mathrm{v}) = 0 \qquad \text{Eq. 40}$$

This equation is called as adjoint equation, and its solution defines adjoint state of equation. The adjoint equation is explicitly expressed with incomplete adjoint approximation from Eq. 34 :

$$\begin{aligned}
\mathrm{D_v} J(\mathbf{v}, \boldsymbol{\lambda}; \delta\mathbf{v}) = & \int_{\Gamma_s} \delta v_x \left(v_x - v_x^{obs}\right) + \delta v_y \left(v_y - v_y^{obs}\right) d\Gamma_s \\
& + \int_{\Omega} \delta v_x \nabla \cdot \left(2\mu \dot{\boldsymbol{\epsilon}}_{\mathbf{1}}(\lambda)\right) \, d\Omega \\
& + \int_{\Omega} \delta v_y \nabla \cdot \left(2\mu \dot{\boldsymbol{\epsilon}}_{\mathbf{2}}(\boldsymbol{\lambda})\right) \, d\Omega \qquad \text{Eq. 41} \\
& - \int_{\partial\Omega} \delta v_X \; 2\mu \dot{\boldsymbol{\epsilon}}_{\mathbf{1}}(\boldsymbol{\lambda}) \; d\Omega - \int_{\partial\Omega} \delta v_y \; 2\mu \dot{\boldsymbol{\epsilon}}_{\mathbf{2}}(\boldsymbol{\lambda}) \; d\Omega \\
& - \int_{\Gamma_b} \alpha^2 \delta v_x \lambda_x d\Gamma - \int_{\Gamma_b} \alpha^2 \delta v_y \lambda_y d\Gamma
\end{aligned}$$

From above equation, incomplete adjoint equation is retrieved as :

$$\begin{aligned}
\nabla \cdot \left(2\mu \dot{\boldsymbol{\epsilon}}_{\mathbf{1}}(\lambda)\right) = 0 \\
\nabla \cdot \left(2\mu \dot{\boldsymbol{\epsilon}}_{\mathbf{2}}(\boldsymbol{\lambda})\right) = 0
\end{aligned} \qquad \text{Eq. 42}$$

, and its boundary conditions are

$$\begin{cases} 2\mu \dot{\boldsymbol{\epsilon}}_{\mathbf{1}}(\lambda) \cdot \boldsymbol{n} = v_x - v_x^{obs} \\ 2\mu \dot{\boldsymbol{\epsilon}}_{\mathbf{2}}(\lambda) \cdot \boldsymbol{n} = v_y - v_y^{obs} \end{cases} \text{ on } \Gamma_\mathrm{s}$$

$$\begin{cases} 2\mu \dot{\boldsymbol{\epsilon}}_{\mathbf{1}}(\lambda) \cdot \boldsymbol{n} = 2\alpha^2 \lambda_x \\ 2\mu \dot{\boldsymbol{\epsilon}}_{\mathbf{2}}(\lambda) \cdot \boldsymbol{n} = 2\alpha^2 \lambda_y \end{cases} \text{ on } \Gamma_\mathrm{b} \qquad \text{Eq. 43}$$

$$\begin{cases} 2\mu \dot{\boldsymbol{\epsilon}}_{\mathbf{1}}(\lambda) \cdot \boldsymbol{n} = 0 \\ 2\mu \dot{\boldsymbol{\epsilon}}_{\mathbf{2}}(\lambda) \cdot \boldsymbol{n} = 0 \end{cases} \text{ on } \Gamma_w$$

, which are similar to boundary conditions in forward problem. The spatial distribution of $\boldsymbol{\lambda}$ for Eq. 38 is derived from Eq. 42 and Eq. 43.

Before using control method, it was important to set the initial value for ice shelf rigidity inversion and ice sheet friction coefficient inversion. If initial guess of friction coefficient was close to the estimated solution, speed of convergence was faster. The initial guess for friction coefficient was introduced as (22)

$$\alpha_{\mathrm{ini}} = \left(\frac{\rho g H \parallel \nabla s \parallel}{\parallel v^{obs} \parallel + \epsilon_v}\right)^{\frac{1}{2}} \qquad \text{Eq. 44}$$

, where $\epsilon_{\mathrm{v}} = 0.1\ \mathrm{m/yr}$ (Morlighem et al., 2013). Each cost function weight is set through trial and error. Here. global weight of each cost function is set as w_1 = 1000, w_2 = 10, and w_3 = 10^{-6}, and first and second weight of cost functions area locally reinforced at region with large ice velocity misfit.

2.3.3. Relaxation

Each data had different resolution set, and interpolating the geometry from grid to mesh had non-smoothing geometry. Also, geometry of ice shelf at David Glacier is poorly known. This geometry anomaly causes the flux divergence at grounding line and ice shelf. Therefore, the thickness inversion should be performed for satisfying the mass conservation (Morlighem et al., 2014). Here, bed geometry data satisfied with mass conservation on ice sheet, not ice shelf, is applied to model. Transient simulation was used to relax geometry and remove non-physical undulation, and results of transient simulation was set as initial condition for transient simulation (Favier et al., 2014; Gillet-Chaulet et al., 2012; Seroussi et al., 2011; Seroussi et al., 2014b)(Table 2). During relaxation process, grounding line was changed and other input forcing variables, such as floating ice melting rate and SMB, were constant. After the results of transient simulation, forcing experiments was performed with each forcing variables. The relaxation and transient simulation model should be stabilized numerically by satisfying specific time step of model. This condition is called as Courant-Friedrichs-Lewy (CFL) condition, which could be defined as

$$\mathrm{Dt} < \frac{1}{2}\left(\frac{u}{Dx} + \frac{v}{Dy}\right) \qquad \text{Eq. 45}$$

, where Dt was a time step to transient simulation, (u, v) was a velocity of x, y direction, and Dx, Dy meant that mesh size of x, y direction. Before simulating model for 50 years under climate forcing conditions, smoothing time was set as 15 years.

Table 2. Relaxation condition of previous studies.

Source	Relaxation time	Grounding line position
Gillet-Chaulet et al. (2012)	50 years	-
Favier et al. (2014)	15 years	Moving
Seroussi et al. (2014b)	10 years	Fixed
Morlighem et al. (2016)	100 years	-
Favier et al. (2016)	50 years	-

2.4. Climate Forcing Scenarios

To identify response of ice velocity and sea level equivalent depending on the climate forcing variables, such as SMB change, floating ice melting rate, and ice front position, transient simulation was performed for 50 years. Ice rigidity is kept constant during the transient simulation. When one of changed forcing variables was applied to initial condition of model, the other parameters were constant during transient simulation. For instance, when changed distribution of SMB is applied to initial condition, floating ice melting rate and ice front position were constant.

SMB was multiplied by 0, 0.5, 1.0, 1.5, 2.0, 2.5, 3.0, 3.5, 4.0 (Table 3). Floating ice melting rate was multiplied specific constant 0.5, 0.75, 1.0, 1.25, 1.5, 2.0 to initial melting rate distribution (Table 3). For instance of forced floating ice melting rate with β =2, maximum floating ice melting rate was 2×20 = 40 m/yr at deep base elevation with -1200 m (Figure 15). Retreat ice front was shown in Figure 16, where Front 1 and 2 are located at ice tongue, Front 3 is positioned at transition zone between ice tongue and internal ice shelf, and other front positions are at ice shelf.

Table 3. This tables showed the forcing parameters during transient simulation

SMB [m/yr]	**Floating ice melting rate [m/yr]**
SMB × 0	Melt × 0.5
SMB × 0.5	Melt × 0.75
SMB × 1.0	Melt × 1.0
SMB × 1.5	Melt × 1.25
SMB × 2.0	Melt × 1.5
SMB × 2.5	Melt × 2.0
SMB × 3.0	
SMB × 3.5	
SMB × 4.0	

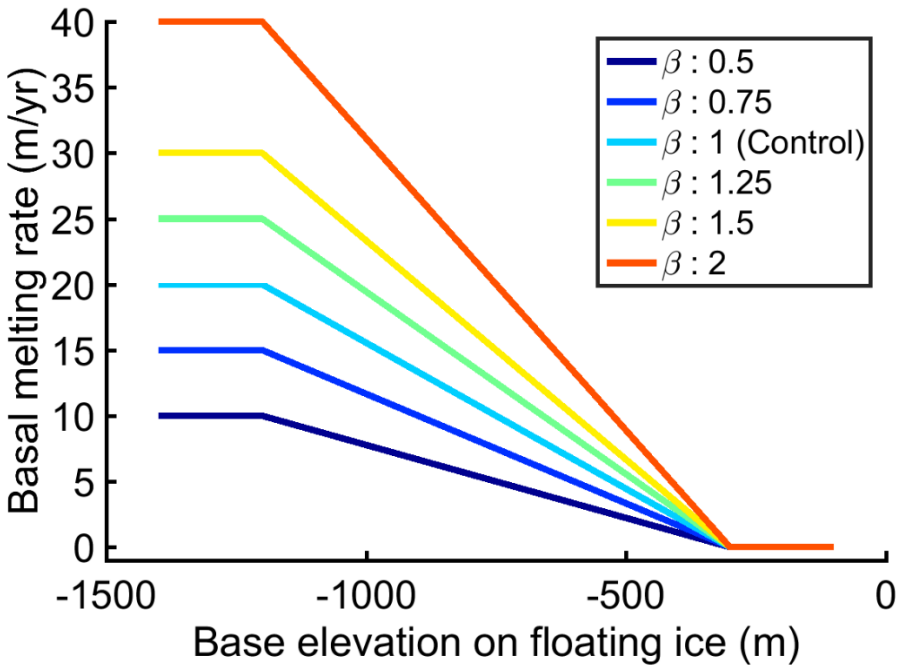

Figure 15. Floating ice melting rate dependent on each forcing multipliers.

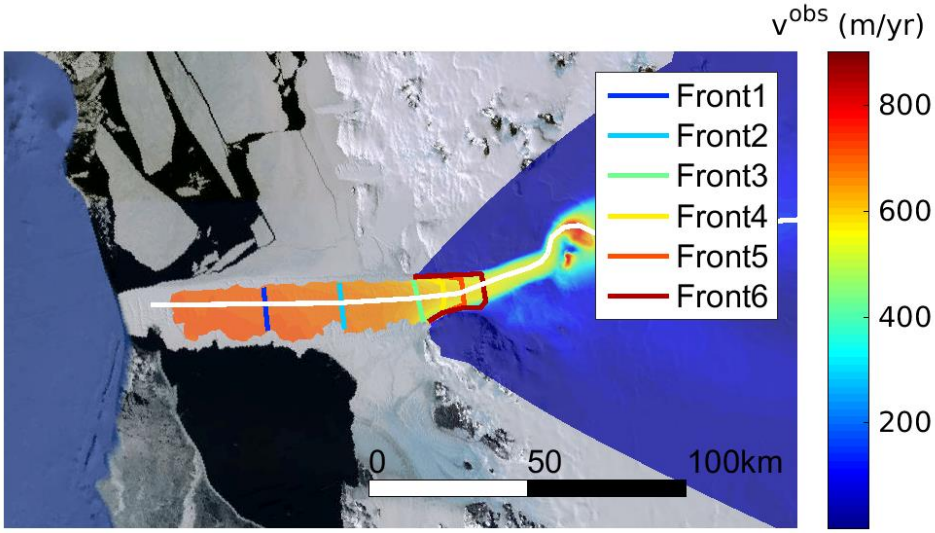

Figure 16. Ice front retreat position is shown on velocity field data. Front 1 and 2 are located at ice tongue, Front 3 is positioned at transition zone between ice shelf and ice tongue, and Front 4, 5, and 6 is located at ice shelf. White line indicates the cross section line of DAG.

3. RESULTS AND DISCUSSION

3.1. Initialization

3.1.1. Inversion Results

Basal friction coefficient beneath ice sheet

Friction coefficient is zero at the ice shelves, and grounded ice of friction coefficient is constrained to range between maximum of 400 and minimum of 1.5 (Figure 17). Pattern of friction coefficient is similar with Morlighem et al. (2013), where friction coefficient is low on region with high velocity, and is high on slow moving ice and divide of glacier. Regularization of cost function makes distribution of friction coefficient smooth. Basal drag, which is inferred from inversion, is highly estimated at ice fall with values of about 500 kPa, where subglacial ridge exists, and low basal drag is estimated at internal ice sheet with values of about 100 kPa (Figure 18).

Ice rigidity on ice shelf

Ice rigidity inversion results reflects best values for minimizing misfit between observed velocity and modeled velocity rather than real values. This makes it possible to determine whether the ice rigidity is soft or rigid. Ice rigidity on ice tongue shows smooth distribution compared to internal ice, and its value with 3.6×10^{8} Pa·$s^{1/3}$ corresponds to an equivalent temperature of -35℃(Figure 9). Estimated ice rigidity on ice tongue is more rigid than air temperature of about -11℃ equivalent to ice rigidity value of 1.5×10^{8} Pa·$s^{1/3}$.

Modeled velocity

Figure 20 shows (a) modeled velocity estimated by SSA using inferred friction coefficient and ice rigidity, and (b) difference between modeled velocity and observed velocity. To evaluate the quality of inversion results, average misfit of ice velocity

$$\overline{\Delta v} = \int_{\Omega} \left| \sqrt{u^2 + v^2} - \sqrt{u_{obs}^2 + v_{obs}^2} \right| d\Omega \qquad \text{Eq. 46}$$

is adopted. Average misfit between modeled velocity and observed velocity is 2.5 m/yr on whole domain, and 42 m/yr for fast ice stream region, where ice velocity is over 50 m/yr (Figure 20(b)). For previous studies, ice velocity misfit of Larour et al. (2005) was 50 m/yr for Ronne ice shelf, West Antarctica, and Morlighem et al. (2010) was 27 m/yr for whole domain and 62 m/yr for fast ice flow region at Pine Island Glacier, West Antarctica.

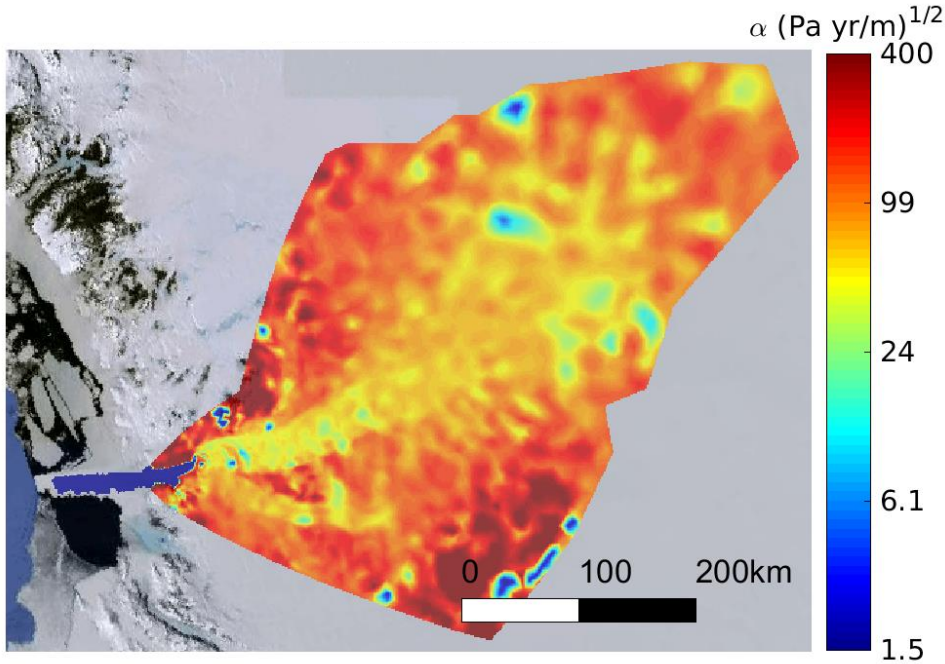

Figure 17. Friction coefficient inferred from inversion method with SSA model.

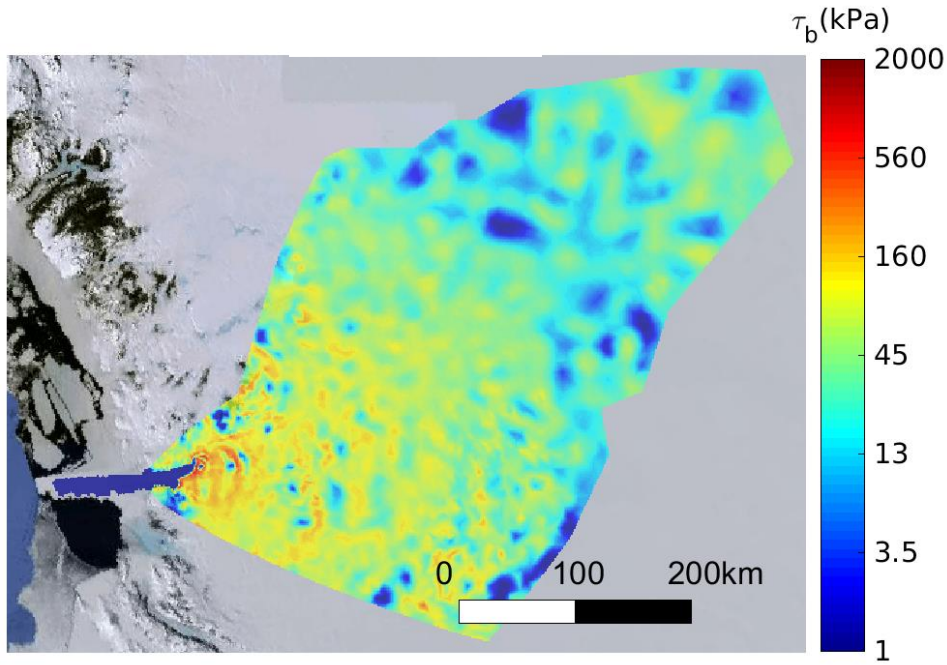

Figure 18. Basal drag ($\tau_b = -\alpha^2 v_b$) of inversion model.

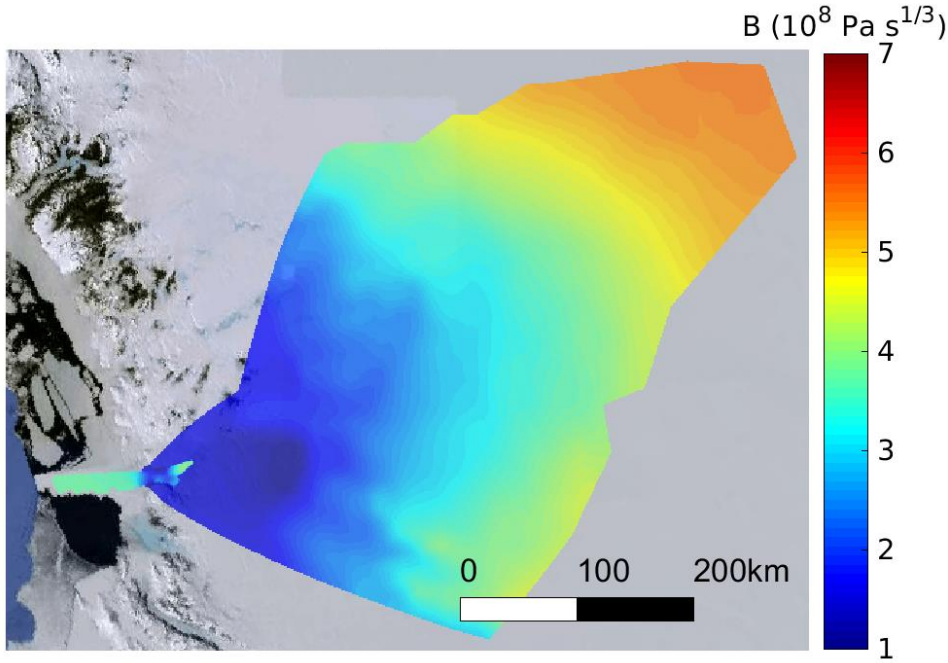

Figure 19. Ice rigidity distribution. Ice rigidity on ice shelf is estimated through inversion model, and assumed by 3D thermal model on ice sheet.

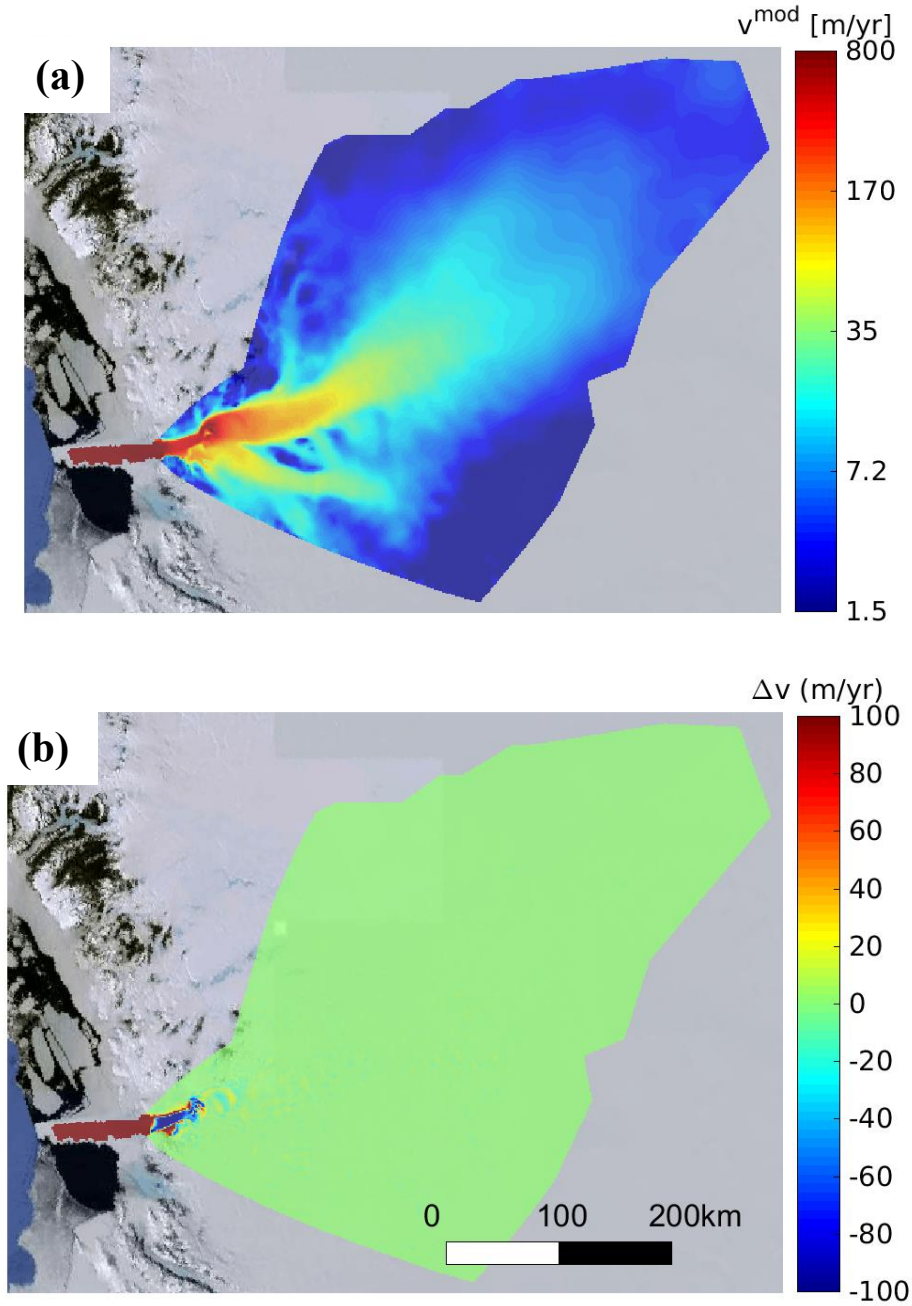

Figure 20. (a) Modeled velocity from inversion method with SSA and (b) velocity difference, where modeled velocity minus observed velocity.

3.1.2. Relaxation Results

The flux divergence not guaranteed near grounding line causes ice velocity changed abruptly at ice front and ice shelf in 1 year transient simulation (Figure 21). Cross section ice velocity after 15 year relaxation is stabilized, compared to 1 years relaxation. Transient simulation is performed for 15 years to stabilize the ice velocity and geometry and reduce the flux divergence. Relaxation velocity for forcing experiments was higher than observed velocity on shear margin, and maximum value of ice velocity peak at ice fall is shifted 10 km toward ice shelf (Figure 23(a)). Also, distortion of ice velocity at ice fall disappears as ice velocity peak moves toward ice shelf, because the flux divergence over 100 m/yr influences ice thickness which is related to ice velocity and driving force of ice(Figure 12(b)). The flux divergence in 15 years near grounding line is reduced 20 m/yr (Figure 22), compared to initial flux divergence of Bedmachine with > 100 m/yr (Figure 12(b)). Ice is accumulated near grounding line, where subglacial ridge exists and basal drag is higher than other areas, however, ice tongue is rarely changed during relaxation (Figure 23(b)). This shift is relatively small and acceptable, considering scale of glacier model system and ice mass change of 0.24% increase. The grounding line along cross section $\overline{AA`}$(Figure 1) is not changed during relaxation because ice sheet is well grounded to the bed.

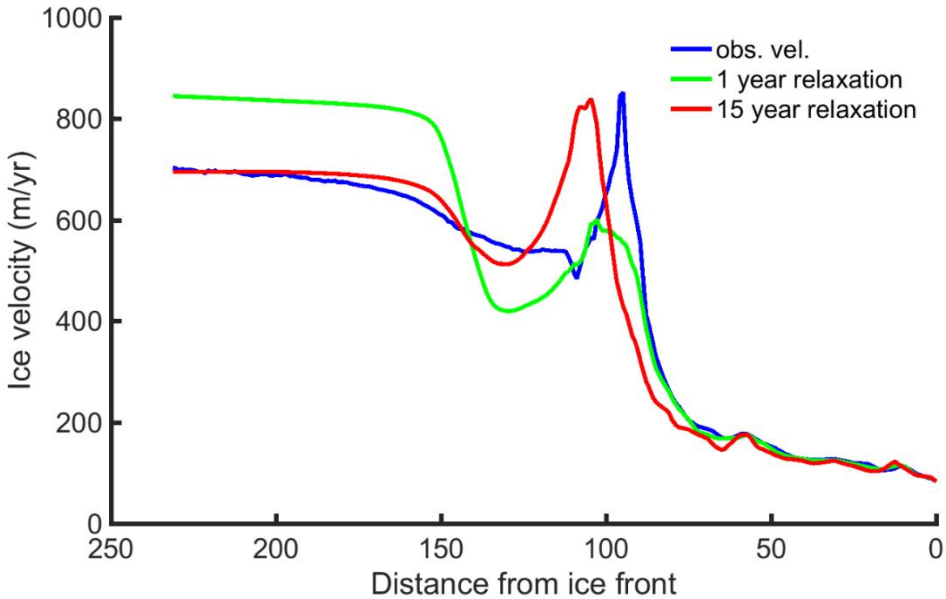

Figure 21. Cross section velocity for observation (blue line), 1 year relaxation (green line), and 15 year (red line) along cross section line ($\overline{AA`}$) on Figure 1(b).

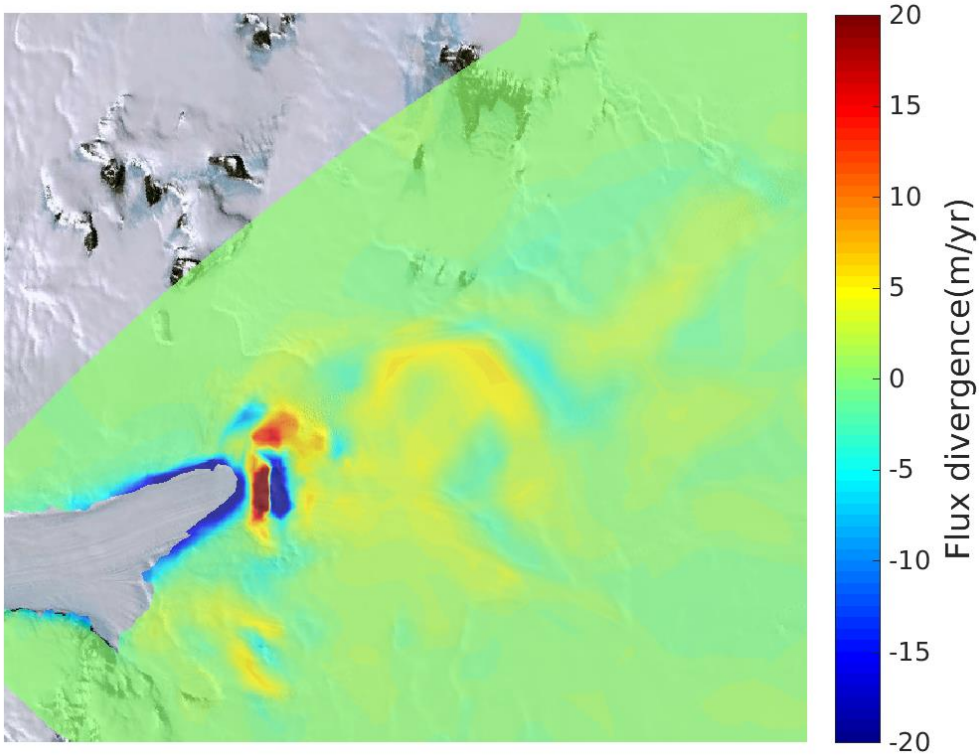

Figure 22. Flux divergence after 15 year relaxation.

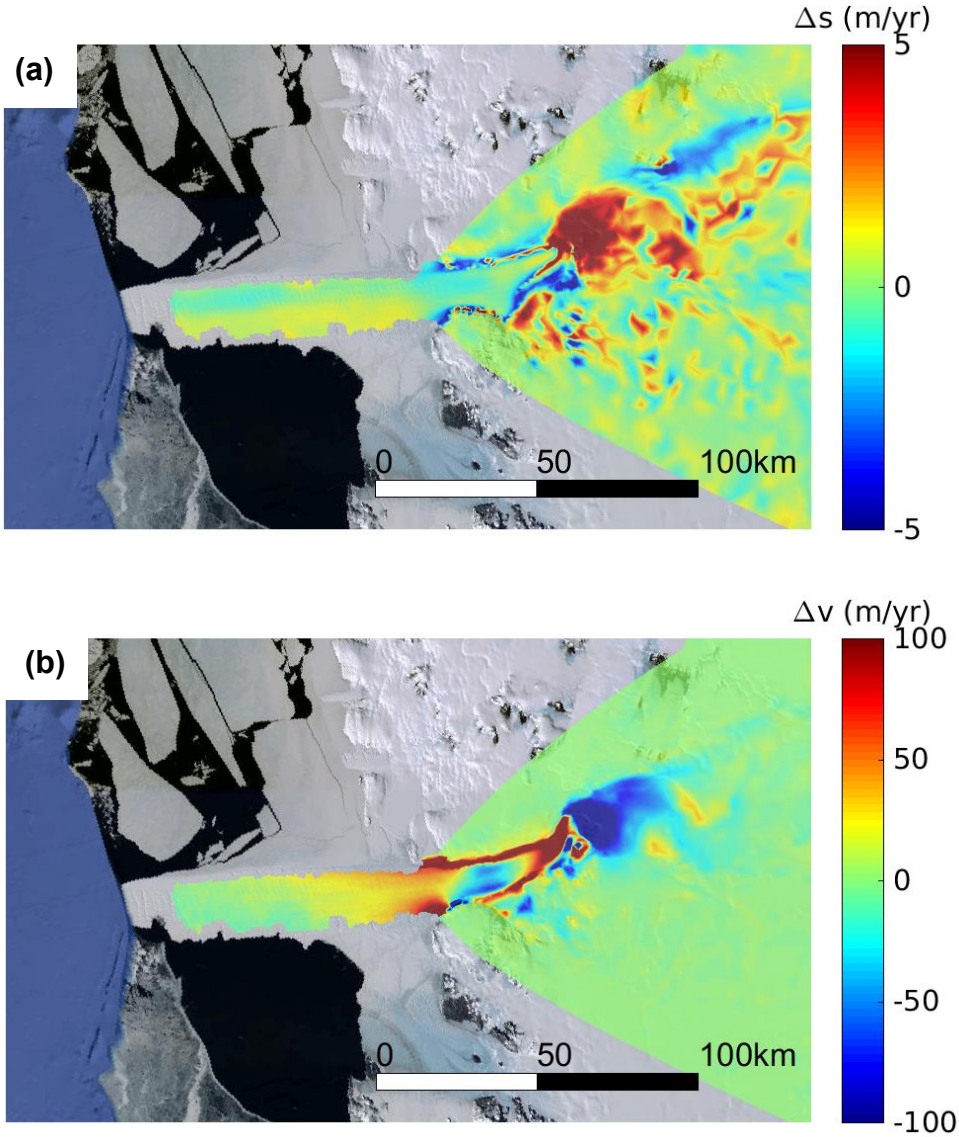

Figure 23. (a) Misfit of ice velocity that 15 year relaxation minus observation velocity, and (b) surface elevation evolution.

3.2. Results of Climate Forcing Scenarios

Control model

Control model means that forcing conditions are not changed during transient simulation, i.g, where surface mass balance multiplier $\alpha = 1$, floating ice melting rate multiplier $\beta = 1$, and ice front isn't retreated. The grounding line isn't changed during control model, and it is located at 130 km from ice front (Figure 24(a)). Ice velocity on ice shelf is rarely accelerated (Figure 24(a)). The sea level equivalent change is about -2.04 mm equivalent with 15 Gt/yr gain of mass for 50 years (Figure 24(b)). Sea level equivalent change is calculated from ice volume above floatation. According to previous study, ice discharge to ocean was estimated as 2 ± 4 Gt/yr (Rignot et al., 2008) and ice discharge was relatively small, compared to other glacier with fast and large ice discharge. Control models at other study area show relatively high ice mass loss of 79.62 Gt/yr at Pine Island Glacier, West Antarctica, and 8.7 Gt/yr at Nioghalvfjerdsfjorden and Zachariae Isstrøm, Greendland (Table 4).

SMB

Scenario of SMB doesn't influence ice velocity dramatically, however, sea level equivalent decreases linearly from -2.0 mm for $\alpha = 1$ to -10.52 mm for $\alpha = 4$ after 50 years (Figure 25(a)). As SMB increases, overall ice thickness on model increases (Figure 26(a)). In case of SMB $\alpha = 4$, the ice thickness near grounding line is about 50 m thicker than control model (Figure 27(a)). Overall increase in ice thickness influences linear increase in above floatation mass.

Floating ice melting rate

After 50 years, increase in floating ice melting rate, with thinning the ice thickness on ice shelf (Figure 26(b)), induces acceleration of ice velocity near grounding line. Acceleration of ice sheet is propagated within which propagates into inland (Figure 25(c)). In all of cases, grounding line is located at about 130 km from ice front. The thickness of ice near grounding line is most thinned with over 200 m compared to control model (Figure 27(b)). The thinning ice thickness depletes buttressing on ice sheet, and ice velocity acceleration propagates inland. The increase of floating ice melting rate shows gradually increase in sea level equivalent from -2.08 to -2.00 mm (Figure 25(d)).

Previous study showed that increase of ocean forcing induced acceleration of ice velocity at ice shelf region by retreating grounding line toward ice sheet (Favier et al., 2014; Seroussi et al., 2014b). In case of study area, the subglacial ridge exists at ice fall, where glacier tributaries are joined, is higher than bed elevation on ice shelf, and it makes grounding line to be unchanged. Therefore, the ice velocity acceleration due to the increase of floating ice melting rate is less than other glaciers.

Retreat of ice front position

Ice front retreat shows that ice tongue (Front 1, 2) doesn't show change in ice velocity. Also, there exists threshold, where retreat of ice shelf (Front 4) doesn't affect ice velocity. When ice front passed by threshold of Front 4, retreat of ice shelf induces acceleration of ice velocity dramatically. These changes in ice velocity influence increase in sea level equivalent, due to decrease in buttressing ice sheet and reducing the lateral confinement at narrow neck of ice shelf. For Front 1 and 2, sea level equivalent after 50 years has the same values of –2.0 mm as control model.

Sea level equivalent for Front 3 and 4 shows change within 0.004 mm compared to the control model, but not significant change. However, sea level equivalent for Front 5 and Front 6 have dramatic increase of values with -2.01 and -1.95 mm.

As ice front position recedes into internal ice shelf, ice thickness is thinned near grounding line, which is located at 130 km from ice front (Figure 26 (c)). Retreat of ice front position and increase in floating ice melting rate show the similar patterns in thinning ice thickness. In case of Front 6 experiment, ice thickness is thinning over 200 m compared to control model, and ice thickness thinning is propagated into internal ice sheet (Figure 27(c)). Other experiments, such as Front 1, 2, 3, 4, do not display dramatic change in ice thickness compared to Front 5 and 6 experiments.

In case of retreat of ice front, ice tongue and some ice shelf region doesn't play a role as buttressing the ice sheet. As previous study mentioned the threshold of ice shelf buttress (Seroussi et al., 2014b), if ice front isn't located at Front 5 or 6, where ice shelf is confined well, ice shelf hardly accelerates the ice shelf. Because capacity of buttress is associated with lateral confinements at shear margin and hard ice rigidity on ice shelf. The lateral confinements on ice tongue can exist due to interacting with ocean, however, it is not sufficient enough to ocean for demonstrating lateral drag.

Passive ice shelf region, where ice shelf area has a little influence on overall ice dynamics, is located at ice tongue (Fürst et al., 2016).The extend PSI of area portion is 49.5%, where extent PSI exists at the middle of Drygalski ice tongue. In this study, PSI isoline is located inward of ice shelf.

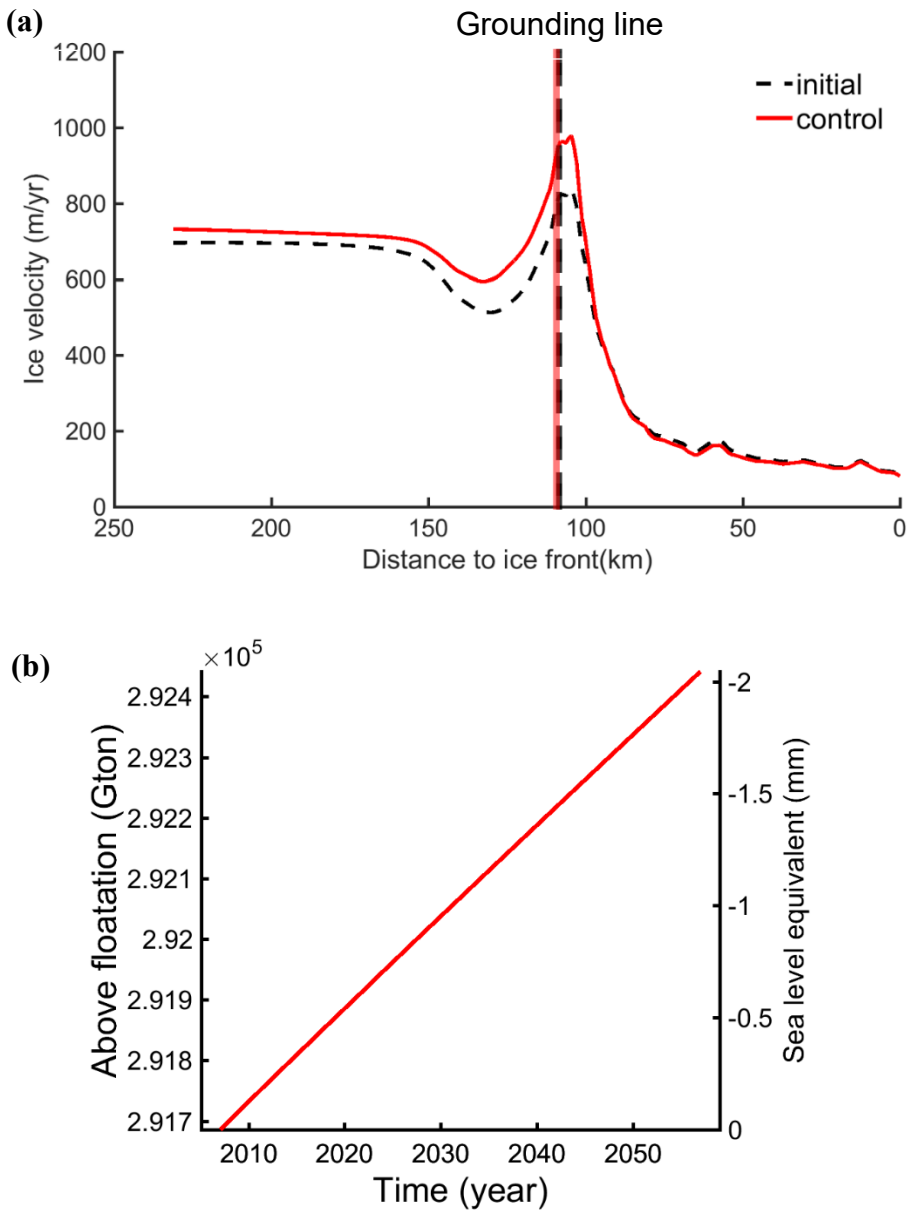

Figure 24. (a) Profile of ice velocity for initial (dash line) and control model with 50 years (red line). Vertical line from ice front with 130 km is grounding line for initial (dash line) and control model (red line). (b) Above floatation change, which is equivalent to sea level equivalent change, for control model.

Table 4. Sea level equivalent of control model

	Seroussi et al. (2014b)	Choi et al. (2017)	In this study
Study Area	Pine Island Glacier, Antarctica	Nioghalvfjerdsfjorden and Zachariae Isstrøm, Greendland	David Glacier, Antarctica
Ice Discharge	79.62 Gt/yr (11 mm)	58.63 Gt/yr (1.2 mm)	-15 Gt/yr (- 2.0 mm)

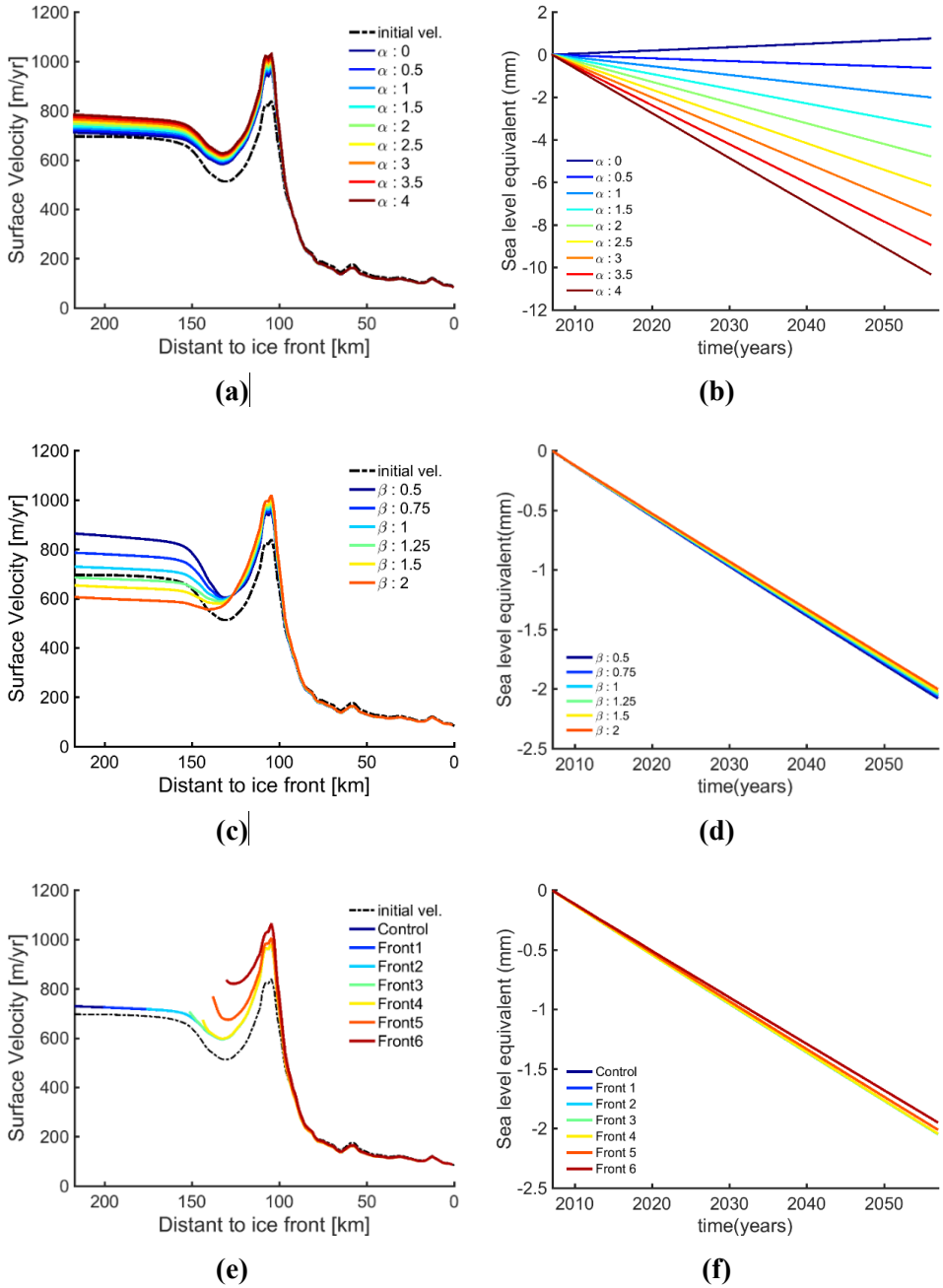

Figure 25. Ice velocity change along cross section line at Drygalski Ice Tongue((a), (c), (e)) and sea level equivalent change((b), (d), (f)) depending on each climate forcing condition.

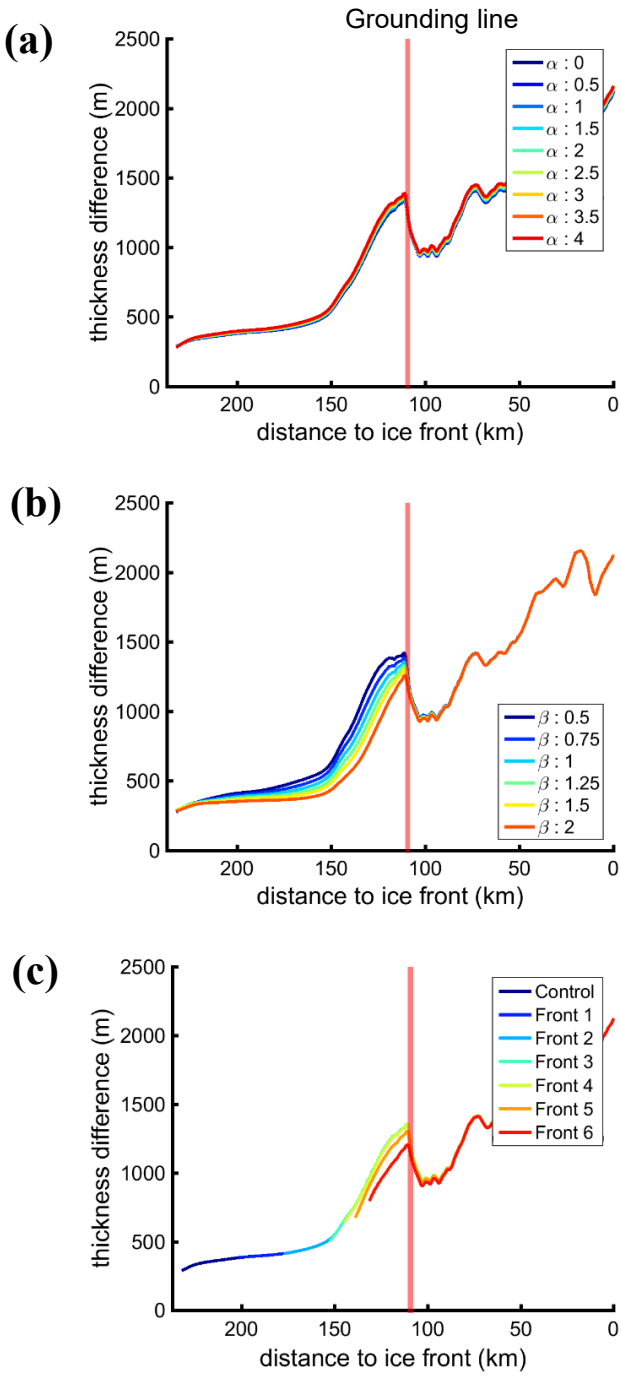

Figure 26. Ice thickness along cross section line shown in Figure 1 in accordance with (a) SMB, (b) floating ice melting rate, and (c) ice front retreat. Vertical red box indicates the grounding line of control model.

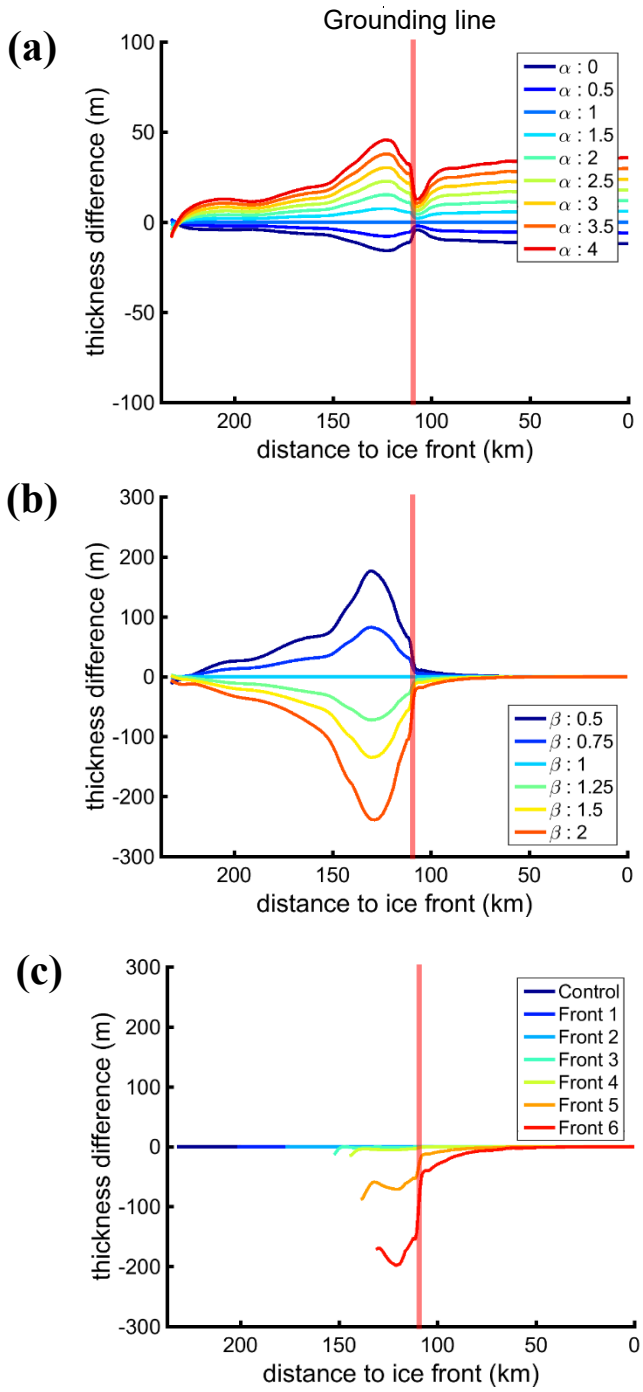

Figure 27. Thickness difference that thickness of forcing experiments minus ice thickness of control model along flow line ($\overline{AA'}$) shown in Figure 1. Vertical red line indicates the grounding line of control model.

Front retreat and floating ice melting

To identify acceleration of ice shelf by increased floating ice melting rate, ice shelf is retreated to Front 6, and various floating ice melting rate is introduced. Although drastic retreat of ice shelf to Front6, increased floating ice melting rate rarely influences the acceleration of ice shelf (Figure 28(a)) compared to experiment of Front 6 retreat without intensified floating ice melting rate (Figure 25(e)). Sea level equivalent of Front 6 retreat with floating ice melting rate $\beta = 2$ is about -1.92 mm, which is slightly larger than Front 6 retreat with $\beta = 1$ of -1.95 mm (Figure 28(b)). In this experiment, an increment in sea level equivalent due to increase in floating ice melting rate with recession of ice front position is not the same as only elevated floating ice melting rate. For instance, in case of experiments with only applied different floating ice melting rate, sea level equivalent difference between control model and $\beta = 2$ is 0.05 mm, which is larger than 0.03 mm of difference between $\beta = 1$ and $\beta = 2$ with Front 6 retreat. The retreat of ice front position elevates the base elevation on ice shelf, and reduces the floating ice melting rate at same location.

As ice thickness on ice shelf decrease (Figure 29(a)), floating ice melting rate dependent on depth of ice shelf decreases linearly. For example, if the initial ice front and the floating ice melting rate $\beta = 2$ are applied to model, the thickness of the glacier near grounding line becomes thin with values of more than 200 m compared to control model, however, Front 6 retreat with $\beta = 2$ becomes thin less than 200 m (Figure 29(b)). From this aspect, it is inferred that study area is more sensitive to ice front position than change in floating ice melting rate. Although high floating ice melting rate is introduced, the effect on ice front position retreat is influential.

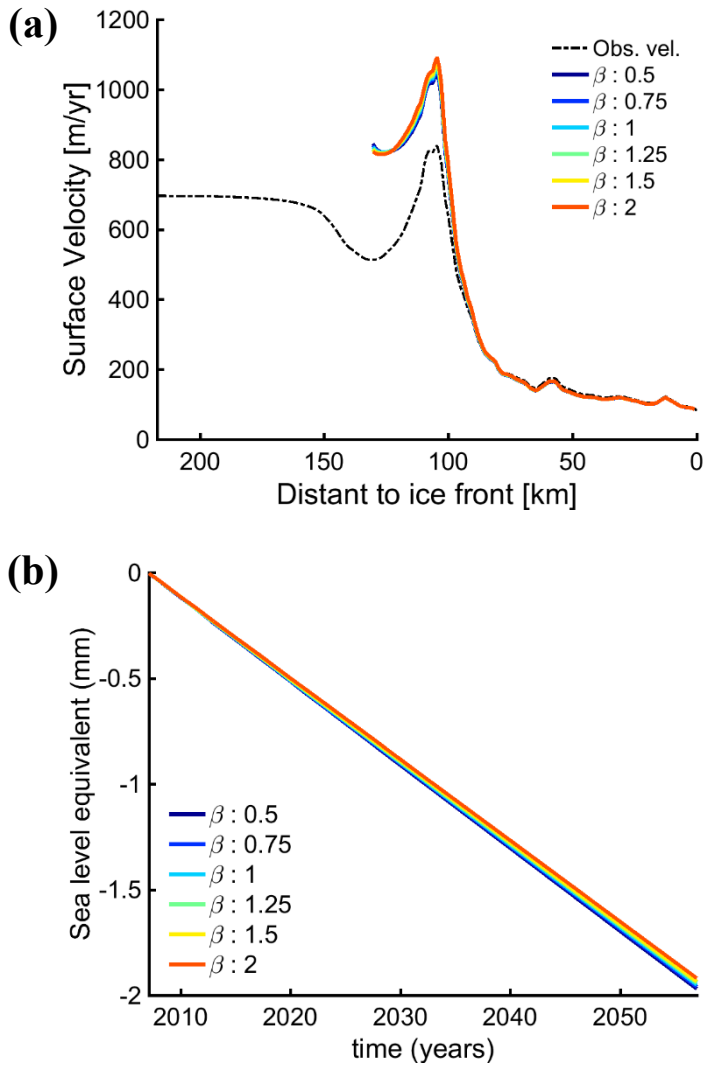

Figure 28. After extracting ice front to Front 6, and different floating ice melting rates are introduced. (a) ice velocity along cross section of Drygalski Ice Tongue ($\overline{AA`}$), and (b) displays the sea level equivalent.

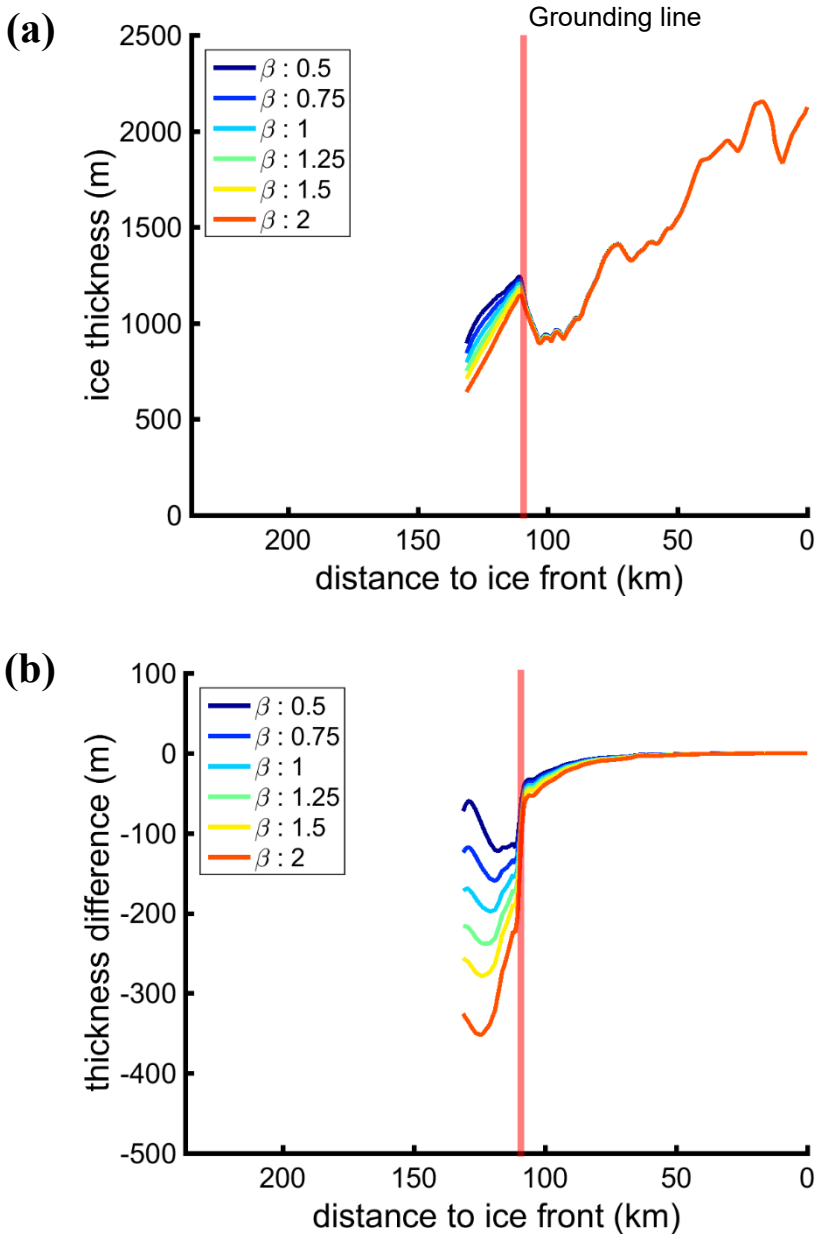

Figure 29. Depending on floating ice melting rate with ice front position retreat to Front 6, (a) ice thickness, and (b) ice thickness difference that ice thickness in terms of floating ice melting rate minus control model along cross section shown in Figure 1.

4. CONCLUSIONS

The 2D Shallow Shelf Approximation model in Ice Sheet System Model (ISSM) was used to constructing the initial conditions of David Glacier (DAG), East Antarctica, and transient simulation were performed with introducing variable climate forcing scenarios, such as i) surface mass balance (SMB), ii) floating ice melting rate, and iii) ice front positions. Results from this study suggests that DAG was stable over 50 year forcing conditions, where net ice discharge showed negative values. For SMB changes, the case studies expect for zero SMB showed the negative ice mass loss. In case of increase in floating ice melting rate and ice front retreat showed the acceleration of ice near grounding line. Bed elevation at ice fall relatively higher than ocean elevation made it difficult for grounding line to retreat toward ice sheet in case of increase of floating ice melting rate and dramatic ice front retreat to 100 km from initial ice front. The retreat of convex ice shelf contacted with ocean did not influence the ice velocity change and sea level equivalent change. Unless the ice shelf was retreated to 80 km from ice front, it did not affect the ice velocity and sea level equivalent, but showed the drastic change when the ice front retreated further inside. Additional experiments with retreat to 100 km from ice front and varying floating ice melting rate was performed to identify the effect of floating ice melting rate to ice shelf buttressing. In that case, twofold floating ice melting rate did not significantly induced acceleration of glacier, and did not change the grounding line. The ice dynamics of DAG was mainly affected by ice front position.

Further Study

The flux divergence did not get solved at ice fall after applying observed thickness

along flight tracks. In this study, there was no thickness data on ice fall applied to thickness inversion so the flux divergence still remained. Additional exploration for measuring thickness or observation data was necessary to reduce the flux divergence near grounding line.

Ice shelf water from melt near grounding line, which is cold and fresh, upwelled, and it refreezes (Wuite et al., 2009). Decrease in pressure induces increase of freezing point of water, and upwelled ice shelf water could be changed into ice, where it is called as 'ice pump'. However, parameterization of melting rate with depth dependent did not consider heterogeneous spatial floating ice melting rate, where deep ocean water upwelling is frozen at transition zone of ice shelf and ice tongue.

SSA model shows weak prediction of grounding line migration, and couldn't capture vertical velocity at ice fall. For capturing more delicate prediction of ice dynamics, HO or FS model should be conducted, which are more precise than 2D SSA model.

5. REFRENCES

Arthern, R. J., Winebrenner, D. P., and Vaughan, D. G., 2006, Antarctic snow accumulation mapped using polarization of 4.3-cm wavelength microwave emission: Journal of Geophysical Research: Atmospheres, v. 111, no. D6.

Barrett, P., 2013, Resolving views on Antarctic Neogene glacial history–the Sirius debate: Earth and Environmental Science Transactions of the Royal Society of Edinburgh, v. 104, no. 01, p. 31-53.

Choi, Y., Morlighem, M., Rignot, E., Mouginot, J., and Wood, M., 2017, Modeling the Response of Nioghalvfjerdsfjorden and Zachariae Isstrøm Glaciers, Greenland, to Ocean Forcing Over the Next Century: Geophysical Research Letters, v. 44, no. 21, p. 11,071-011,079.

Comiso, J. C., 2000, Variability and trends in Antarctic surface temperatures from in situ and satellite infrared measurements: Journal of Climate, v. 13, no. 10, p. 1674-1696.

Cuffey, K. M., and Paterson, W. S. B., 2010, The physics of glaciers, Academic Press.

DeConto, R. M., and Pollard, D., 2016, Contribution of Antarctica to past and future sea-level rise: Nature, v. 531, no. 7596, p. 591-597.

Fürst, J. J., Durand, G., Gillet-Chaulet, F., Tavard, L., Rankl, M., Braun, M., and Gagliardini, O., 2016, The safety band of Antarctic ice shelves: Nature Climate Change, v. 6, no. 5, p. 479-482.

Favier, L., Durand, G., Cornford, S. L., Gudmundsson, G. H., Gagliardini, O., Gillet-Chaulet, F., Zwinger, T., Payne, A., and Le Brocq, A. M., 2014, Retreat of Pine Island Glacier controlled by marine ice-sheet instability: Nature Climate Change, v. 4, no. 2, p. 117-121.

Favier, L., Pattyn, F., Berger, S., and Drews, R., 2016, Dynamic influence of pinning points on marine ice-sheet stability: a numerical study in

Dronning Maud Land, East Antarctica: The Cryosphere, v. 10, no. 6, p. 2623.

Fretwell, P., Pritchard, H. D., Vaughan, D. G., Bamber, J., Barrand, N., Bell, R., Bianchi, C., Bingham, R., Blankenship, D., and Casassa, G., 2013, Bedmap2: improved ice bed, surface and thickness datasets for Antarctica: The Cryosphere, v. 7, no. 1.

Frezzotti, M., and Mabin, M., 1994, 20th century behaviour of Drygalski Ice Tongue, Ross Sea, Antarctica: Annals of Glaciology, v. 20, no. 1, p. 397-400.

Gillet-Chaulet, F., Gagliardini, O., Seddik, H., Nodet, M., Durand, G., Ritz, C., Zwinger, T., Greve, R., and Vaughan, D. G., 2012, Greenland ice sheet contribution to sea-level rise from a new-generation ice-sheet model: The Cryosphere, v. 6, no. 6, p. 1561-1576.

Glen, J. W., The creep of polycrystalline ice, *in* Proceedings Proceedings of the Royal Society of London A: Mathematical, Physical and Engineering Sciences1955, Volume 228, The Royal Society, p. 519-538.

Hecht, F., 1998, BAMG: bidimensional anisotropic mesh generator: User Guide. INRIA, Rocquencourt.

Larour, E., Rignot, E., Joughin, I., and Aubry, D., 2005, Rheology of the Ronne Ice Shelf, Antarctica, inferred from satellite radar interferometry data using an inverse control method: Geophysical Research Letters, v. 32, no. 5.

Larour, E., Seroussi, H., Morlighem, M., and Rignot, E., 2012, Continental scale, high order, high spatial resolution, ice sheet modeling using the Ice Sheet System Model (ISSM): Journal of Geophysical Research: Earth Surface, v. 117, no. F1.

MacAyeal, D. R., 1989, Large-scale ice flow over a viscous basal sediment: Theory and application to ice stream B, Antarctica: Journal of Geophysical Research: Solid Earth, v. 94, no. B4, p. 4071-4087.

MacAyeal, D. R., 1993, A tutorial on the use of control methods in ice-sheet modeling: Journal of Glaciology, v. 39, no. 131, p. 91-98.

Massimo, F., 1993, Glaciological study in Terra Nova Bay, Antarctica,

inferred from remote sensing analysis: Annals of Glaciology, v. 17, no. 1, p. 63-71.

Morlighem, M., Bondzio, J., Seroussi, H., Rignot, E., Larour, E., Humbert, A., and Rebuffi, S., 2016, Modeling of Store Gletscher's calving dynamics, West Greenland, in response to ocean thermal forcing: Geophysical Research Letters, v. 43, no. 6, p. 2659-2666.

Morlighem, M., Rignot, E., Mouginot, J., Seroussi, H., and Larour, E., 2014, High-resolution ice-thickness mapping in South Greenland: Annals of Glaciology, v. 55, no. 67, p. 64-70.

Morlighem, M., Rignot, E., Seroussi, H., Larour, E., Ben Dhia, H., and Aubry, D., 2010, Spatial patterns of basal drag inferred using control methods from a full-Stokes and simpler models for Pine Island Glacier, West Antarctica: Geophysical Research Letters, v. 37, no. 14.

Morlighem, M., Seroussi, H., Larour, E., and Rignot, E., 2013, Inversion of basal friction in Antarctica using exact and incomplete adjoints of a higher-order model: Journal of Geophysical Research: Earth Surface, v. 118, no. 3, p. 1746-1753.

Mouginot, J., Scheuchl, B., and Rignot, E., 2012, Mapping of ice motion in Antarctica using synthetic-aperture radar data: Remote Sensing, v. 4, no. 9, p. 2753-2767.

Pattyn, F., 2003, A new three-dimensional higher-order thermomechanical ice sheet model: Basic sensitivity, ice stream development, and ice flow across subglacial lakes: Journal of Geophysical Research: Solid Earth, v. 108, no. B8.

Pattyn, F., and Durand, G., 2013, Why marine ice sheet model predictions may diverge in estimating future sea level rise: Geophysical research letters, v. 40, no. 16, p. 4316-4320.

Pittard, M., Galton-Fenzi, B., Roberts, J., and Watson, C., 2016, Organization of ice flow by localized regions of elevated geothermal heat flux: Geophysical Research Letters, v. 43, no. 7, p. 3342-3350.

Rignot, E., 2002, Mass balance of East Antarctic glaciers and ice shelves from satellite data: Annals of Glaciology, v. 34, no. 1, p. 217-227.

Rignot, E., Bamber, J. L., Van Den Broeke, M. R., Davis, C., Li, Y., Van De Berg, W. J., and Van Meijgaard, E., 2008, Recent Antarctic ice mass loss from radar interferometry and regional climate modelling: Nature geoscience, v. 1, no. 2, p. 106-110.

Rignot, E., and Jacobs, S. S., 2002, Rapid bottom melting widespread near Antarctic ice sheet grounding lines: Science, v. 296, no. 5575, p. 2020-2023.

Rignot, E., Velicogna, I., van den Broeke, M. R., Monaghan, A., and Lenaerts, J. T., 2011, Acceleration of the contribution of the Greenland and Antarctic ice sheets to sea level rise: Geophysical Research Letters, v. 38, no. 5.

Scambos, T. A., Bohlander, J., Shuman, C. u., and Skvarca, P., 2004, Glacier acceleration and thinning after ice shelf collapse in the Larsen B embayment, Antarctica: Geophysical Research Letters, v. 31, no. 18.

Schlegel, N. J., Larour, E., Seroussi, H., Morlighem, M., and Box, J., 2015, Ice discharge uncertainties in Northeast Greenland from boundary conditions and climate forcing of an ice flow model: Journal of Geophysical Research: Earth Surface, v. 120, no. 1, p. 29-54.

Schoof, C., 2007, Marine ice-sheet dynamics. Part 1. The case of rapid sliding: Journal of Fluid Mechanics, v. 573, p. 27-55.

Seroussi, H., Morlighem, M., Larour, E., Rignot, E., and Khazendar, A., 2014a, Hydrostatic grounding line parameterization in ice sheet models: Cryosphere, v. 8, no. 6.

Seroussi, H., Morlighem, M., Rignot, E., Larour, E., Aubry, D., Ben Dhia, H., and Kristensen, S. S., 2011, Ice flux divergence anomalies on 79north Glacier, Greenland: Geophysical Research Letters, v. 38, no. 9.

Seroussi, H., Morlighem, M., Rignot, E., Mouginot, J., Larour, E., Schodlok, M., and Khazendar, A., 2014b, Sensitivity of the dynamics of Pine

Island Glacier, West Antarctica, to climate forcing for the next 50 years: Cryosphere, v. 8, no. 5.

Shapiro, N. M., and Ritzwoller, M. H., 2004, Inferring surface heat flux distributions guided by a global seismic model: particular application to Antarctica: Earth and Planetary Science Letters, v. 223, no. 1, p. 213-224.

Swithinbank, C., 1988, Antarctica, US Government Printing Office, v. 1386.

Van Der Veen, C. J., and Whillans, I., 1989, Force budget: I. Theory and numerical methods: Journal of Glaciology, v. 35, no. 119, p. 53-60.

Vaughan, D. G., Comiso, J. C., Allison, I., Carrasco, J., Kaser, G., Kwok, R., Mote, P., Murray, T., Paul, F., Ren, J., Rignot, R., Solomina, O., Steffen, K., and Zhang, T., 2013, Observations: Cryosphere. In: Climate Change 2013.

Wuite, J., Jezek, K., Wu, X., Farness, K., and Carande, R., 2009, The velocity field and flow regime of David Glacier and Drygalski Ice Tongue, Antarctica: Polar Geography, v. 32, no. 3-4, p. 111-127.

국문 초록

전지구적 기온이 상승함에 따라 빙하의 유출에 의한 해수면 상승이 얼마만큼 상승할지 관심이 높아지고 있다. 서남극은 근래 가장 많은 빙하의 유출이 발생하는 지역이다. 그에 반해 동남극은 빙상의 기저면이 해수면 보다 높아 상대적으로 안정적이지만 해수면 상승의 잠재력(sea level rise potential)이 서남극에 비해 10배 이상 높다. 동남극에 위치한 David Glacier은 남극대륙횡단 산맥(Transantarctic Mountains)의 계곡에서 피요르드 형식으로 빙하가 형성되어 바다로 유출되는 지역으로 80 km 길이의 Drygalski Ice Tongue이 길게 자란 지역이다. 빙붕 기저면의 녹는 양의 증가 및 빙하 전면부의 위치 변화는 해수로 빙하 유출을 가속화시키는 요인들이며, 적설량은 빙하의 질량을 일정하게 유지시켜 주는 요소 중에 하나이다. 본 연구에서는 Ice Sheet System Model의 2D Shallow Shelf Approximation 모델을 이용하여 역산 방법을 통해 비정상 모델(transient model)의 빙하 기저면의 마찰 계수(friction coefficient) 및 빙하의 강성(ice rigidity)에 해당하는 값을 추정하였다. 이후, 적설량, 빙붕 기저면의 녹는 양 및 빙하 전면부의 위치를 변경하면서 50 년간 해수면 상승 기여분 및 빙하의 속도 변화를 관찰하였다. 그 결과, 역산 방법을 통해 구한 기저면 응력은 빙저 돌출부(subglacial ridge)가 존재하는 아이스 폴(ice fall) 지역에서 크게 계산 되었다. 현재와 같은 조건으로 50 년간 지속되는 모델(제어 모델, control model)의 경우, 연간 15 Gton 가량 질량이 꾸준히 상승하는 것으로 나타났으며, 이는 빙하 유출아 많은 지역 중 하나인 Pine Island Glacier에 비해 안정적인 것이다. 현재 빙하 전면부로부터 90 km 이상 후퇴할 경우, 제어 모델에 비해 최대 1 Gton/yr의 질량 감소가 나타났으며, 최대 빙붕 기저면의 녹는 양 증가의 경우는 0.4 Gt/yr의 질량 감소를 보였다. 이러한 변화는 빙하접지면(grounding line)에서의 속도 변화와 연관이 있으며, 최대 빙하 전면부 후퇴가 가장 큰 속도의 증가를 보였다. 또한, 일정 수준 이하의 빙하 전면부 후퇴는 빙하 속도 및 빙하 상승 기여분 변화에 영향을 미치지 못하는 것으로 나타났다.

주요어 : 데이비드 빙하, 해수면 상승 기여분 변화, 빙하 기저면 용융, 빙하 전면부 후퇴, Shallow Shelf Approximation model.